The Astrophysical Journal Supplement Series, 268:15 (19pp), 2023 September https://doi.org/10.3847/1538-4365/acdcfd
© 2023. The Author(s). Published by the American Astronomical Society.
OPEN ACCESS

The JWST Resolved Stellar Populations Early Release Science Program. II. Survey Overview

Daniel R. Weisz[1], Kristen B. W. McQuinn[2], Alessandro Savino[1], Nitya Kallivayalil[3], Jay Anderson[4], Martha L. Boyer[4], Matteo Correnti[5,6], Marla C. Geha[7], Andrew E. Dolphin[8,9], Karin M. Sandstrom[10], Andrew A. Cole[11], Benjamin F. Williams[12], Evan D. Skillman[13], Roger E. Cohen[2], Max J. B. Newman[2], Rachael Beaton[4,14,15], Alessandro Bressan[16], Alberto Bolatto[17,18], Michael Boylan-Kolchin[19], Alyson M. Brooks[2,20], James S. Bullock[21], Charlie Conroy[22], M. C. Cooper[21], Julianne J. Dalcanton[12,20], Aaron L. Dotter[23], Tobias K. Fritz[3], Christopher T. Garling[3], Mario Gennaro[4,24], Karoline M. Gilbert[24], Léo Girardi[25], Benjamin D. Johnson[22], L. Clifton Johnson[26], Jason S. Kalirai[27], Evan N. Kirby[28], Dustin Lang[29], Paola Marigo[30], Hannah Richstein[3], Edward F. Schlafly[4], Judy Schmidt[31], Erik J. Tollerud[4], Jack T. Warfield[3], and Andrew Wetzel[32]

[1] Department of Astronomy, University of California, Berkeley, CA 94720, USA; dan.weisz@berkeley.edu
[2] Department of Physics and Astronomy, Rutgers, The State University of New Jersey, 136 Frelinghuysen Road, Piscataway, NJ 08854, USA
[3] Department of Astronomy, University of Virginia, 530 McCormick Road, Charlottesville, VA 22904, USA
[4] Space Telescope Science Institute, 3700 San Martin Drive, Baltimore, MD 21218, USA
[5] INAF Osservatorio Astronomico di Roma, Via Frascati 33, I-00078 Monteporzio Catone, Rome, Italy
[6] ASI-Space Science Data Center, Via del Politecnico, I-00133 Rome, Italy
[7] Department of Astronomy, Yale University, New Haven, CT 06520, USA
[8] Raytheon Technologies, 1151 E. Hermans Road, Tucson, AZ 85756, USA
[9] Steward Observatory, University of Arizona, 933 N. Cherry Avenue, Tucson, AZ 85719, USA
[10] Center for Astrophysics and Space Sciences, Department of Physics, University of California San Diego, 9500 Gilman Drive, La Jolla, CA 92093, USA
[11] School of Natural Sciences, University of Tasmania, Private Bag 37, Hobart, Tasmania 7001, Australia
[12] Department of Astronomy, University of Washington, P. O. Box 351580, U.W., Seattle, WA 98195-1580, USA
[13] University of Minnesota, Minnesota Institute for Astrophysics, School of Physics and Astronomy, 116 Church Street SE, Minneapolis, MN 55455, USA
[14] Department of Astrophysical Sciences, Princeton University, 4 Ivy Lane, Princeton, NJ 08544, USA
[15] The Observatories of the Carnegie Institution for Science, 813 Santa Barbara Street, Pasadena, CA 91101, USA
[16] SISSA, Via Bonomea 265, I-34136 Trieste, Italy
[17] Department of Astronomy, University of Maryland, College Park, MD 20742, USA
[18] Joint Space-Science Institute, University of Maryland, College Park, MD 20742, USA
[19] Department of Astronomy, The University of Texas at Austin, 2515 Speedway, Stop C1400, Austin, TX 78712-1205, USA
[20] Center for Computational Astrophysics, Flatiron Institute, 162 Fifth Avenue, New York, NY 10010, USA
[21] Department of Physics and Astronomy, University of California, Irvine, CA 92697 USA
[22] Center for Astrophysics | Harvard & Smithsonian, Cambridge, MA 02138, USA
[23] Department of Physics and Astronomy, Dartmouth College, 6127 Wilder Laboratory, Hanover, NH 03755, USA
[24] The William H. Miller III Department of Physics & Astronomy, Bloomberg Center for Physics and Astronomy, Johns Hopkins University, 3400 N. Charles Street, Baltimore, MD 21218, USA
[25] Padova Astronomical Observatory, Vicolo dell'Osservatorio 5, Padova, Italy
[26] Center for Interdisciplinary Exploration and Research in Astrophysics (CIERA) and Department of Physics and Astronomy, Northwestern University, 1800 Sherman Avenue, Evanston, IL 60201, USA
[27] John Hopkins Applied Physics Laboratory, 11100 Johns Hopkins Road, Laurel, MD 20723, USA
[28] Department of Physics, University of Notre Dame, Notre Dame, IN 46556, USA
[29] Perimeter Institute for Theoretical Physics, Waterloo, ON N2L 2Y5, Canada
[30] Department of Physics and Astronomy G. Galilei, University of Padova, Vicolo dell'Osservatorio 3, I-35122 Padova, Italy
[31] 2817 Rudge Place, Modesto, CA 95355, USA
[32] Department of Physics and Astronomy, University of California, Davis, CA 95616, USA
Received 2023 January 13; revised 2023 June 5; accepted 2023 June 7; published 2023 August 24

Abstract

We present the JWST Resolved Stellar Populations Early Release Science (ERS) program. We obtained 27.5 hr of NIRCam and NIRISS imaging of three targets in the Local Group (Milky Way globular cluster M92, ultrafaint dwarf galaxy Draco II, and star-forming dwarf galaxy WLM), which span factors of $\sim 10^5$ in luminosity, $\sim 10^4$ in distance, and $\sim 10^5$ in surface brightness. We describe the survey strategy, scientific and technical goals, implementation details, present select NIRCam color–magnitude diagrams (CMDs), and validate the NIRCam exposure time calculator (ETC). Our CMDs are among the deepest in existence for each class of target. They touch the theoretical hydrogen-burning limit in M92 ($<0.08\ M_\odot$; $M_{\rm F090W} \sim +13.6$), include the lowest-mass stars observed outside the Milky Way in Draco II ($0.09\ M_\odot$; $M_{\rm F090W} \sim +12.1$), and reach ~ 1.5 mag below the oldest main-sequence turnoff in WLM ($M_{\rm F090W} \sim +4.6$). The PARSEC stellar models provide a good qualitative match to the NIRCam CMDs, though they are ~ 0.05 mag too blue compared to M92 F090W − F150W data. Our CMDs show detector-dependent color offsets ranging from ~ 0.02 mag in F090W – F150W to ~ 0.1 mag in F277W – F444W; these appear to be due to differences in the zero-point calibrations among the detectors. The NIRCam ETC

Original content from this work may be used under the terms of the Creative Commons Attribution 4.0 licence. Any further distribution of this work must maintain attribution to the author(s) and the title of the work, journal citation and DOI.

(v2.0) matches the signal-to-noise ratios based on photon noise in uncrowded fields, but the ETC may not be accurate in more crowded fields, similar to what is known for the Hubble Space Telescope. We release the point-source photometry package DOLPHOT, optimized for NIRCam and NIRISS, for the community.

Unified Astronomy Thesaurus concepts: Stellar photometry (1620); Local Group (929); Stellar populations (1622); Hertzsprung Russell diagram (725); James Webb Space Telescope (2291)

1. Introduction

The resolved stellar populations of nearby galaxies are central to a wide range of astrophysics. The observed colors, luminosities, and spectral features of resolved stars in galaxies within the Local Volume (LV) anchor our knowledge of star formation (e.g., star cluster formation, the initial mass function (IMF), and the importance of binarity; Massey 2003; McKee & Ostriker 2007; Sarajedini et al. 2007; Bastian et al. 2010; Sana et al. 2012; Kroupa et al. 2013; Krumholz 2014; Piotto et al. 2015; Krumholz et al. 2019), stellar feedback (e.g., the interplay between stars and their immediate surroundings; e.g., Oey 1996; Dohm-Palmer et al. 1998; Stinson et al. 2006, 2007; Governato et al. 2010; Ostriker et al. 2010; Lopez et al. 2011; Pellegrini et al. 2011; Lopez et al. 2014; El-Badry et al. 2016; McQuinn et al. 2018, 2019b), dust production and characteristics (e.g., Gordon et al. 2003; Boyer et al. 2006, 2010; Meixner et al. 2010; Dalcanton et al. 2015; Schlafly et al. 2016; Green et al. 2019; Gordon et al. 2021; Yanchulova Merica-Jones et al. 2021), and stellar chemistry and kinematics across a wide range of environments (e.g., Venn et al. 2004; Simon & Geha 2007; Geha et al. 2009; Kirby et al. 2011; Collins et al. 2013; Vargas et al. 2013; Gilbert et al. 2014; Vargas et al. 2014; Ji et al. 2016; Gilbert et al. 2019b; Escala et al. 2020; Kirby et al. 2020; Gilbert et al. 2022). Resolved stars are the basis for the local distance ladder (e.g., Freedman et al. 2001; Riess et al. 2011; Beaton et al. 2016; Riess et al. 2016; McQuinn et al. 2017b, 2019a; Freedman et al. 2020; Riess et al. 2022), which provides constraints on the expansion of the Universe and the nature of dark energy (e.g., Di Valentino et al. 2021). They anchor our knowledge of the stellar evolution models that are used to interpret the light of distant galaxies (e.g., Dotter et al. 2008; Girardi et al. 2010; Bressan et al. 2012; Ekström et al. 2012; VandenBerg et al. 2012; Choi et al. 2016; Eldridge et al. 2017; Conroy et al. 2018; Hidalgo et al. 2018; Eldridge & Stanway 2022) and provide detailed insight into the dynamic assembly of our Galactic neighborhood, cosmic reionization, the first stars, near-field cosmology, and the nature of dark matter on the smallest scales (e.g., Mateo 1998; Tolstoy et al. 2009; Weisz et al. 2014a; Brown et al. 2014; Boylan-Kolchin et al. 2015; Frebel & Norris 2015; Gallart et al. 2015; McQuinn et al. 2015; Wetzel et al. 2016; Starkenburg et al. 2017a; Bullock & Boylan-Kolchin 2017; Kallivayalil et al. 2018; McConnachie et al. 2018; Conroy et al. 2019; Simon 2019; Patel et al. 2020; Boylan-Kolchin & Weisz 2021; Sacchi et al. 2021; Pearson et al. 2022; McQuinn et al. 2023).

Over the past ∼30 yr, much of this science has been enabled by the Hubble Space Telescope (HST). Since its first images of resolved stars in the local Universe (e.g., Paresce et al. 1991; Campbell et al. 1992; Guhathakurta et al. 1992; Freedman et al. 1994; Hunter et al. 1995), HST's exquisite sensitivity, angular resolution, and broad wavelength coverage have transformed our knowledge of the Universe by observing hundreds of nearby galaxies for thousands of hours (e.g., Freedman et al. 2001; Brown et al. 2006; Holtzman et al. 2006; Dalcanton et al. 2009, 2012b; Brown et al. 2012; Gallart et al. 2015; Riess et al. 2016; Skillman et al. 2017; Tully et al. 2019; Williams et al. 2021), including the Panchromatic Hubble Andromeda Treasury (PHAT) program, which resolved 100 million stars across the disk of M31 (Dalcanton et al. 2012a; Williams et al. 2014).

However, while HST continues to catalyze new astrophysical insights in nearby galaxies, it has only scratched the surface of science enabled by infrared (IR) observations. Compared to the UV and optical, HST's IR camera has coarser angular resolution, which limits it to brighter stars due to stellar crowding, and it can only observe a small portion of the IR spectrum, which limits the types of stellar populations it can study.

JWST will be transformative for resolved stellar populations in the IR. Compared to any other facility, JWST will resolve individual stars at larger distances, to fainter luminosities, over wider color baselines, in more crowded areas, and in regions of higher extinction. JWST can provide the first main-sequence turnoff (MSTO)-based star formation histories (SFHs) of galaxies beyond the Local Group (LG; e.g., Weisz & Boylan-Kolchin 2019), systematically measure the subsolar mass stellar IMF directly from star counts as a function of environment (e.g., Geha et al. 2013; Kalirai et al. 2013; El-Badry et al. 2017; Gennaro et al. 2018a; Filion et al. 2020; Gennaro & Robberto 2020), determine proper motions (PMs) and orbital histories for dozens of galaxies outside our immediate Galactic neighborhood (e.g., van der Marel et al. 2012; Kallivayalil et al. 2013; Sohn et al. 2013; Zivick et al. 2018; Sohn et al. 2020; Warfield et al. 2023), construct parsec-scale maps of the interstellar medium (ISM) in galaxies out to several megaparsecs (e.g., Dalcanton et al. 2015; Gordon et al. 2016; Yanchulova Merica-Jones et al. 2017, 2021), establish a new anchor to the physics of the evolved stars that dominate the rest-frame near-IR light of distant galaxies (e.g., Maraston et al. 2006; Melbourne et al. 2012; Boyer et al. 2015, 2019), provide high-fidelity distances to galaxies throughout the LV (e.g., Beaton et al. 2016; McQuinn et al. 2017a, 2019a; Tully et al. 2019; Freedman et al. 2020; Riess et al. 2022), and much more.

With these remarkable capabilities in mind, we have undertaken the JWST Resolved Stellar Populations Early Release Science (ERS) Program (DD-1334; PI: D. Weisz) to establish JWST as the premier facility for the study of resolved stellar populations in the IR such that it can match and exceed HST's successes in the local Universe. To realize this goal, our ERS program has acquired deep multiband NIRCam and NIRISS imaging of three targets in the LG: one Milky Way globular cluster (GC; M92), one ultrafaint dwarf galaxy (UFD; Draco II), and one distant star-forming dwarf galaxy (WLM). These diverse targets showcase a broad range of the science described above and enable the development and testing of JWST-specific modules for the widely used crowded field stellar photometry package DOLPHOT (Dolphin 2000, 2016).

In this paper, we summarize the design of our ERS program, illustrate the new JWST-specific capabilities of DOLPHOT,

outline the photometric reduction process, present a first look at JWST observations of our targets, and undertake select comparisons with stellar models and the current JWST exposure time calculator (ETC). Papers in preparation by our team will provide a detailed overview of the new NIRCam and NIRISS modules for DOLPHOT and will focus on a wide variety of science results enabled by the ERS data beyond what is described here.

This paper is organized as follows. We summarize the program's overarching science and technical aims and target selection in Section 2. We then describe how we translated these goals into an observational strategy in Section 3. We detail the actual ERS observations in Section 4 and summarize the application of DOLPHOT in Section 5. In Section 6 we present NIRCam color–magnitude diagrams (CMDs) and compare them to select stellar models and evaluate the performance of NIRCam ETC. We summarize our program in Section 7.

2. Program Goals

Our team developed a set of main science and technical goals based on anticipated common community use cases of JWST for resolved stellar populations. For simplicity, we limited our considerations to science cases based on imaging with NIRCam, which is considered the "workhorse" camera of JWST, as well as NIRISS imaging, which we used in parallel. This setup is analogous to the commonly used mode of HST in which the Advanced Camera for Surveys (ACS)/Wide Field Camera (WFC) operates as the primary instrument with WFC3/UVIS acquiring imaging in parallel (e.g., Dalcanton et al. 2012b; Gallart et al. 2015; Skillman et al. 2017; Albers et al. 2019; Williams et al. 2021).

Science based on the imaging of resolved stars often requires stellar photometry in crowded fields. Because of that, resolved stellar population studies are technically daunting, requiring highly optimized observations and sophisticated analysis tools that have been developed and refined over the past ∼40 yr (e.g., Buonanno et al. 1979; Tody 1980; Stetson 1987; Schechter et al. 1993; Stetson 1994; Anderson & King 2000; Dalcanton et al. 2012a; Williams et al. 2014). A main technical goal of our program is to develop and release NIRCam and NIRISS modules for DOLPHOT, along with practical recommendations and demonstrations for applying DOLPHOT to NIRCam and NIRISS imaging. Here, we summarize our main science goals, technical goals, and science "deliverables" which guide our ERS program.

2.1. Scientific Goals

Our team identified six main science themes that guided the construction of our ERS program. They are:

1. *SFHs.* A galaxy's resolved stellar content encodes its SFH, which can be reconstructed by fitting CMDs with stellar evolution models (e.g., Tosi et al. 1989; Tolstoy 1996; Harris & Zaritsky 2001; Dolphin 2002; Hidalgo et al. 2009). These SFHs are particularly robust when CMDs extend below the oldest MSTO (e.g., Gallart et al. 2005). The faintness of this feature in the optical ($M_V \sim +4$) has limited current "gold standard" SFHs to galaxies within the LG. However, the relatively low effective temperatures of these stars, combined with the decreased sky background in the near-IR and JWST's excellent sensitivity and angular resolution, will enable it to measure the first SFHs based on the oldest MSTOs for galaxies outside the LG (e.g., Weisz & Boylan-Kolchin 2019; JWST-GO-1617, PI: K. McQuinn) from which outstanding questions (e.g., the effects of reionization and/or environment on galaxy formation) can be uniquely addressed (e.g., Bullock & Boylan-Kolchin 2017; Simon 2019). Our JWST program will showcase JWST's ability to measure robust SFHs.
2. *The subsolar mass IMF.* Resolved star counts shows that the lowest-mass galaxies appear to have subsolar IMF slopes which deviate from the Galactic value (e.g., Geha et al. 2013; Kalirai et al. 2013; Gennaro et al. 2018b). However, even with HST, it has proven challenging to acquire sufficiently deep data (down to $\sim 0.2\,M_\odot$; El-Badry et al. 2017; Gennaro et al. 2018a, 2018b) to confirm these putative IMF variations unambiguously. Our ERS program will illustrate JWST's capabilities for definitively measuring the subsolar IMF in a ultrafaint MW satellite, paving the way for a systematic study of the low-mass IMF and star formation in extreme environments.
3. *PMs.* High-precision astrometry enables the measurement of PMs throughout the LG. Gaia has been transformative for objects in the MW halo, while HST has laid the foundation for fainter, more distant systems. JWST is the future of precision astrometry for faint and/or more distant objects. On its own, and in tandem with Gaia, HST, and Roman, JWST imaging will provide measurements of the total masses, dark-matter profiles, and orbital histories for ∼100 galaxies in and around the LG (e.g., Kallivayalil et al. 2015; Bullock & Boylan-Kolchin 2017; Fritz et al. 2018; Gilbert et al. 2019a; Battaglia et al. 2022; Warfield et al. 2023). Our ERS program will showcase the PM measurements capabilities of JWST.
4. *Evolved stars.* Cool evolved stars such as red supergiants and asymptotic giant branch (AGB) stars are responsible for 20%–70% of the rest-frame near-IR luminosity of star-forming galaxies (e.g., Maraston et al. 2006; Melbourne et al. 2012) and are sites of dust production (e.g., Ventura et al. 2001). However, the rapid evolution of dusty AGB stars is challenging to model (e.g., Maraston et al. 2006; Girardi et al. 2010; Conroy 2013; Marigo et al. 2017), which has only begun to be alleviated by recent observations (e.g., Boyer et al. 2015, 2017). JWST's expansive IR filter set will reveal elusive dust-enshrouded populations of AGB stars (e.g., oxygen-rich M stars and carbon-rich C stars) across a wide range of galactic environments (e.g., Hjort et al. 2016; Jones et al. 2017; Marini et al. 2020). Our ERS program will demonstrate JWST's capacity to study IR-bright, evolved stars.
5. *Extinction mapping.* In the LG, Spitzer and Herschel have mapped dust emission at ∼10″–40″ and ∼7″–12″ resolution, respectively (10 pc for the Magellanic Clouds; 100 pc for M31 and M33; Draine & Li 2007; Gordon et al. 2014; Chastenet et al. 2019; Utomo et al. 2019). JWST can map the cold ISM at significantly higher spatial resolution by inferring dust content from its impact on stellar spectral energy distributions (SEDs; e.g., Dalcanton et al. 2015; Gordon et al. 2016). Our ERS

observations will demonstrate JWST's ability to map dust extinction and relate it to properties of the cold ISM.

6. *Ages of GCs.* Accurate ages of the oldest GCs are particularly important for connecting the stellar fossil record to events in the early Universe, including cosmic reionization and the age of the Universe itself (e.g., Chaboyer et al. 1996; Grebel & Gallagher 2004; Ricotti & Gnedin 2005; Monelli et al. 2010; Weisz et al. 2014b; Brown et al. 2014; Boylan-Kolchin et al. 2015). Current age estimates are typically limited to $\sim$1 Gyr precision (i.e., twice as long as reionization lasted) due to the age–metallicity degeneracies at the MSTO (see Boylan-Kolchin & Weisz 2021 and references therein). JWST observations of the "kink" on the lower main sequence (MS) can yield more precise estimates of cluster ages (e.g., Sarajedini et al. 2009; Bono et al. 2010; Kalirai et al. 2012; Correnti et al. 2018). Our ERS data will showcase the powerful capabilities of JWST for precise GC age dating.

Beyond enabling our main science goals, we sought to identify observations that would make our ERS program rich for archival pursuits. Examples include measuring extragalactic distances in JWST bands (e.g., tip of the red giant branch (TRGB) and variable stars; Beaton et al. 2016; Madore et al. 2018; McQuinn et al. 2019a), identifying rare stars from low-mass metal-poor stars to luminous red supergiants (e.g., Schlaufman & Casey 2014; Casey & Schlaufman 2015; Levesque 2018), searching for dust production among red giant branch stars (RGB; e.g., Boyer et al. 2006, 2010), and examining the nature of dark matter using wide binaries (e.g., Peñarrubia et al. 2016).

2.2. Technical Goals

The main technical goal of our ERS program is to enable resolved star science by the broader community. At the heart of this goal is the addition of NIRCam and NIRISS modules to DOLPHOT. This process includes the technical development of NIRCam and NIRISS modules for DOLPHOT, testing their performance on real data, releasing data products that immediately enable science (e.g., stellar catalogs), and providing guidance to the community on best use practices of DOLPHOT for future applications. Here, we broadly describe each of these technical goals and how they influenced the observational strategy of our ERS program.

As with previous updates to DOLPHOT (e.g., Dalcanton et al. 2012b; Dolphin 2016; and many unpublished updates), the core functionality of the code remains the same as described in Dolphin (2000), but certain aspects have been updated for NIRCam and NIRISS.

The DOLPHOT modules for NIRCam and NIRISS each feature their own preprocessing routines that apply masks (e.g., of reference, saturated, and other unusable pixels) to the images based on the data quality flags provided by the STScI pipeline. They also apply the pixel area maps appropriate to each camera. Other updates include the use of photometric calibrations provided in the image metadata, conversions to VEGAMAG, and camera-specific point-spread function (PSF) models with corresponding encircled energy corrections.

For testing DOLPHOT on real data, we identified several observational scenarios that we anticipate to be common for NIRCam and NIRISS studies of resolved stars. They are:

1. Targets with various levels of crowding. This includes images that are completely uncrowded (e.g., in which aperture versus PSF photometry can be compared), images with highly variable amounts of crowding (e.g., due to surface brightness variations), and highly crowded images (i.e., the photometric depth is primarily limited by crowding).
2. Targets that include stars spanning a large dynamic range in brightness in the same image. An example would be a GC, in which there are very bright red giants and extremely faint dwarfs. This enables a variety of tests, including the ability to recover faint sources next to very bright objects.
3. Targets with bright, saturated stars. JWST is extremely sensitive. Understanding the degree to which saturated stars affect the photometry of fainter objects will be important to a variety of science goals.
4. Targets that demonstrate the ability of using the higher angular resolution short-wavelength (SW) images to increase the accuracy of the long-wavelength (LW) photometry. PHAT showed that joint reduction of HST optical and IR data produced IR photometry that provides significantly sharper CMDs compared to reducing IR data alone (e.g., Williams et al. 2014). Similar gains should be possible with NIRCam.
5. Targets that enable the simultaneous reduction of HST and JWST imaging. To date, DOLPHOT has produced wonderful cross-camera results for HST (e.g., Dalcanton et al. 2012a; Williams et al. 2014, 2021), but it needs to be vetted and optimized for cross-facility use.

2.3. Deliverables

Our program is in the process of providing several "deliverables" to the community that can be found on our team website[33] and on MAST as high-level science products (doi:10.17909/cn6n-xg90). A primary deliverable is the public release of DOLPHOT with NIRCam- and NIRISS-specific modules for which "beta" versions can be found on the main DOLPHOT website.[34] This software enables crowded field stellar photometry for a diverse range of science in the local Universe. Along with the software release we will provide extensive documentation of how to use DOLPHOT and examples of it applied to our ERS observations. Following careful calibration and testing, we will release high-level science products including the output of our team DOLPHOT runs on ERS data (e.g., diagnostic plots and files), and NIRCam and NIRISS stellar catalogs for each target along with artificial star tests (ASTs). These data products will be refined as our understanding of JWST improves (e.g., due to updated PSF models) and will eventually include examples of how to use DOLPHOT for the simultaneous reduction of HST and JWST imaging.

3. Strategy

3.1. Filters

The diversity of our science cases required careful consideration of filter selection. Several of our science goals are centered around maximizing depth, color baseline, and

[33] https://ers-stars.github.io
[34] http://americano.dolphinsim.com/dolphot/

astrometric precision. Accordingly, we primarily focused on SW filter selection, which has better sensitivity (for most stars) and angular resolving power than the LW channel.

Using an ancient, metal-poor isochrone (12.5 Gyr, [Fe/H] = −2.0) from the MIST stellar models (Choi et al. 2016), we examined the expected performance for SW wide filter (F070W, F090W, F115W, F150W, and F200W) permutations at three different CMD locations: the blue horizontal branch (HB; $T_{\rm eff} \sim 7000$ K), the MSTO ($T_{\rm eff} \sim 6000$ K), and the lower MS ($\sim 0.2\,M_\odot$; $T_{\rm eff} \sim 4000$ K). At each point, we used the precommissioning JWST ETC (v1.1.1) to compute the exposure time required to reach a signal-to-noise ratio (S/N) = 10 for the "scene" in the ETC.

The best performing filters for our areas of consideration are F090W, F115W, and F150W. They all exhibit comparable performance at the HB and MSTO. However, F090W requires 2.5 times more exposure time to achieve the same S/N for a $0.2\,M_\odot$ star as either F115W or F150W. Nevertheless, we opted for F090W over F115W because compared to F115W − F150W, F090W − F150W provides superior color information for most stars and F090W has the potential for higher angular resolution (if dithered appropriately), which is critical for astrometry. Finally, the similarity between F090W and HST/F814W (or Johnson *I* band) provides useful features such as matching catalogs between facilities and TRGB distance determinations (e.g., McQuinn et al. 2019a). F070W and F200W provide the largest color baseline, but each filter is less sensitive to stars far from their effective wavelength. For example, F070W required four times more integration time for a $0.2\,M_\odot$ star than the next bluest filter, F090W. F200W requires twice as much exposure time for an HB star than F150W.

We opted to use the same F090W − F150W filter combination for all targets to provide for an empirical comparison between GCs and UFDs (e.g., Brown et al. 2012) and for good sampling of the oldest MSTO in distant dwarf galaxies. We considered more than two SW filters, but the cost of acquiring extra data outweighed the scientific utility. We selected simultaneously observed LW filters on a per target basis, as they enable secondary science unique to each object. Finally, we selected F090W and F150W for parallel NIRISS imaging for consistency with NIRCam.

We emphasize that while our filter combinations represent a good compromise across the CMD for our program goals, they may not be optimal for all science cases. We encourage exploration tailored to a program's particular science aims.

3.2. Target Selection

We selected targets by first considering all known GCs in the MW (Harris 2010) and galaxies within ∼1 Mpc (McConnachie 2012), including updates to both catalogs and discoveries through 2017 (e.g., Laevens et al. 2014, 2015b; Bechtol et al. 2015; Drlica-Wagner et al. 2015; Koposov et al. 2015). The limiting distance was selected to ensure we could reach the oldest MSTO with an S/N =10 in the most distant system in a reasonable amount of time based on previous experience with HST (e.g., Cole et al. 2014; Albers et al. 2019) and results from the JWST ETC.

We required that each target have extensive HST imaging (e.g., to enable combined HST and JWST PM studies and create panchromatic stellar catalogs) and have a good sampling of ground-based spectra (e.g., for full phase space information, comparing stellar properties from spectra and photometry, and incorporating stellar abundance patterns into various analyses).

Table 1
Basic Observational Properties of the Three ERS Targets

	M92	Draco II	WLM
R.A. (J2000)	$17^{\rm h}17^{\rm m}07^{\rm s}.27$	$15^{\rm h}52^{\rm m}47^{\rm s}.60$	$00^{\rm h}01^{\rm m}58^{\rm s}.16$
Decl. (J2000)	$+43^{\rm d}08^{\rm m}11^{\rm s}.5$	$+64^{\rm d}33^{\rm m}55^{\rm s}.0$	$-15^{\rm d}27^{\rm m}39^{\rm s}.34$
M_V (mag)	−8.2	−0.8	−14.2
$E(B-V)$ (mag)	0.02	0.01	0.03
$(m-M)_0$ (mag)	14.6	16.9	24.9
μ_0 (mag arcsec^{-2})	15.5	28.1	24.8
r_h (′)	1.0	2.7	7.8

Note. Properties for M92 have been taken from the updated MW GC catalog of Harris (2010), while those of Draco II and WLM are from the LG galaxy catalog of McConnachie (2012). Note that μ_0 is the effective surface brightness and r_h is the half-light radius.

We then identified a minimum set of targets that could be used to achieve our science and technical goals: one MW GC, one UFD, and one more distant star-forming dwarf galaxy. We then sought to maximize observational efficiency by focusing on some of the nearest examples of these classes. We eliminated targets that were not visible during the nominal ERS window.

This selection process yielded three targets: MW GC M92, MW satellite UFD Draco II, and star-forming dwarf galaxy WLM. Basic observational characteristics of these targets are listed in Table 1. We detail the observational strategy for each target in the following sections.

3.3. M92

M92 (NGC 6341) is a well-studied, metal-poor GC in the MW that is often used as a benchmark for extragalactic stellar population studies and for photometric calibration (e.g., to verify zero-points; e.g., Dalcanton et al. 2009; Brown et al. 2014; Gallart et al. 2015). Imaging this system satisfies several science and technical goals, including GC ages, individual star PMs, and the present day mass function, testing DOLPHOT over a large dynamic range of stellar brightness and spatially varying stellar density, and gauging the effects of bright saturated stars on the photometric process.

As illustrated in Figure 1, we placed the NIRCam field near the center of M92, with the aim of maximizing NIRCam spatial overlap with a wealth of multiband HST images of M92. The parallel NIRISS field is located at ∼5 half-light radii. We constrained the orientation such that the NIRISS field had a modest probability of overlapping at least some HST data in the outer regions. However, orientations allowed by the final ERS window did not result in overlap between NIRISS and HST imaging.

We chose the F090W, F150W, F277W, and F444W filters for our NIRCam imaging of M92. We selected F277W and F444W for their broad scientific utility, including studying the lower MS kink at long wavelengths (e.g., Sarajedini et al. 2009; Bono et al. 2010), searching for dust production at low metallicities (e.g., Boyer et al. 2006, 2010), and exploring multiple populations in the IR (e.g., Milone et al. 2012, 2014; Correnti et al. 2016; Milone et al. 2017).

We aimed to reach an S/N = 10 at $0.1\,M_\odot$ in F090W and F150W, which we estimate to be $m_{F090W} \approx 26$ ($M_{\rm F090W} \approx +11.4$) and $m_{\rm F150W} \approx 25.8$ ($M_{\rm F150W} \approx +11.2$) based on MIST

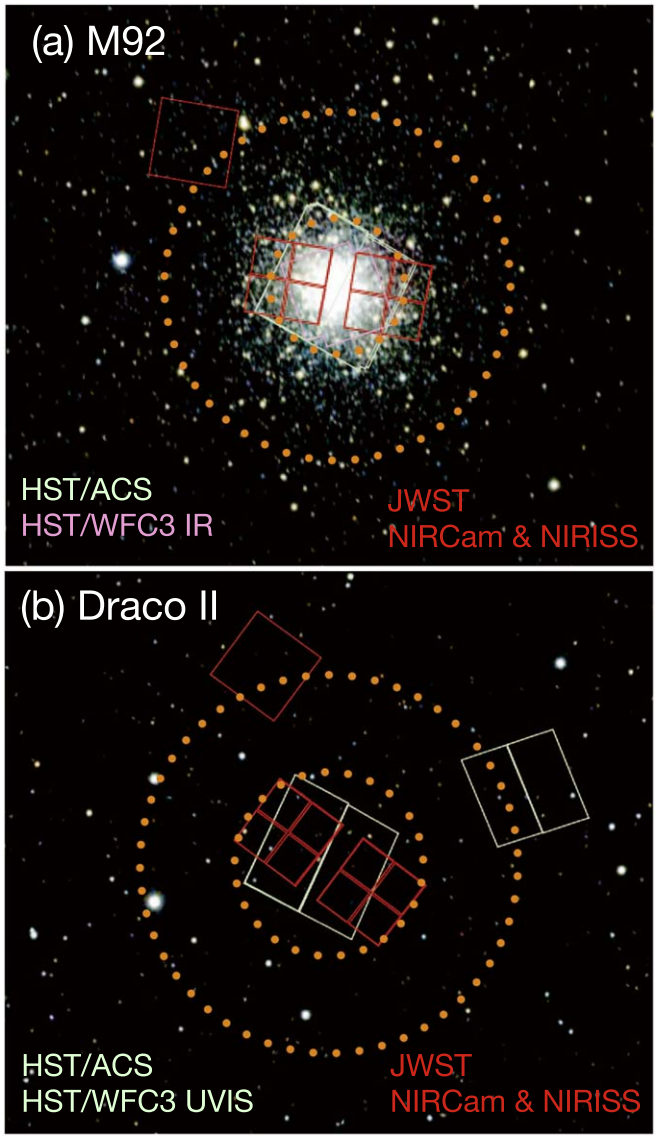

Figure 1. The locations of our M92 and Draco II NIRcam and NIRISS observations (plotted in red) for each ERS target, overplotted on a Pan-STARRS optical image. The orange dotted lines indicate 2 and 5 half-light radii (r_h) for M92 and 1 and 2 r_h for Draco II. We show additional pointings for each system: (a) M92: select HST optical (green; HST-GO-10775) and IR (pink; HST-GO-11664). (b) Draco II: HST/ACS optical data (HST-GO-14734; PI: Kallivayalil) are shown in green. We opted not to undertake large dithers to fill the NIRCam chip and module gaps, which would have substantially increased the program time while only marginally enhancing our science goals.

isochrones and the characteristics of M92 listed in Table 1. The 2017 versions of the ETC (v1.1.1) and the Astronomer's Proposal Tool (APT; v25.1.1) yielded exposure times of 1288 s in each filter. The anticipated S/Ns in the LW filters at $m_{\rm F090W} \approx 26$ were 21.1 in F277W and 6.4 in F444W. We estimated the NIRISS imaging to be marginally shallower than NIRCam with integration times of 1074 s in each of F090W and F150W. The difference in durations is set by facility overheads as calculated by APT.

3.4. Draco II

At ~20 kpc, Draco II is one of the nearest examples of an MW satellite (Laevens et al. 2015a; Longeard et al. 2018). At the time of program design, Draco II was designated as a UFD (i.e., it has dark matter; Willman & Strader 2012; Martin et al. 2016). In the interim, there has been some debate in the literature over its status as a UFD versus GC (e.g., whether or not it has dark matter, a metallicity spread, and the slope of its subsolar stellar mass function; e.g., Longeard et al. 2018; Baumgardt et al. 2022), an issue our JWST data should help resolve.

Draco II's close proximity provides for efficient JWST imaging that reaches far down the lower MS ($\lesssim 0.2\,M_\odot$). Our deep Draco II data satisfy several of our science goals, including measuring the low-mass stellar IMF (which can shed insight into its status as a GC or UFD), determining the SFH of an ancient sparsely populated system, measuring the PMs of individual faint stars using HST and JWST, and exploring our ability to distinguish between faint stars and unresolved background galaxies.

We placed the NIRCam field on the center of Draco II (Figure 1). The field overlaps with archival HST imaging obtained in 2017 March (GO-14734; PI: N. Kallivayalil), Keck spectroscopy, and is well matched to the half-light radius. To maximize scheduling opportunities, we did not constrain the orientation. The NIRISS field is unlikely to contain many Draco II member stars, so its exact placement was not crucial. The primary use of the NIRISS data will be to aid with modeling contamination (e.g., foreground stars and background galaxies) in the F090W − F150W CMD, e.g., as part of measuring the low-mass IMF.

We selected the F090W, F150W, F360M, and F480M filters for our NIRCam imaging of Draco II. The rationale for the two SW filters is described in Section 3.3. The LW filters are located near metallicity-sensitive molecular features in the mid-IR, and they may be suitable for measuring photometric metallicities of metal-poor stars (e.g., Schlaufman & Casey 2014; Casey & Schlaufman 2015) similar to what is possible in the optical using, for example, the calcium H and K lines (e.g., Starkenburg et al. 2017a; Fu et al. 2022). For NIRISS, we used the F090W and F150W filters.

Our target depth is set by low-mass IMF science. Tightly constraining the low-mass IMF in Draco II requires reaching stars $\lesssim 0.2\,M_\odot$ (e.g., El-Badry et al. 2017) with an S/N = 10 in F090W and F150W. Using MIST stellar models and the observational properties of Draco II listed in Table 1, our target depths are S/N ~ 10 at $m_{\rm F090W} = 27$ ($M_{\rm F090W} = +10.3$) and $m_{\rm F150W} = 26.8$ ($M_{\rm F150W} = +10.1$). Using the 2017 versions of the ETC (v1.1.1) and APT (v25.1.1) we found exposure times of 12798 s in F090W and 6399 s in F150W would reach these depths. We opted on SW/LW combinations of F090W/F480M and F150W/F360M, which provided S/Ns of ~7 (F360M) and ~4 (F480M) at F150W = 25. We estimated the NIRISS imaging to have 12,540 s in F090W and 6270 s in F150W, which will result in marginally shallower CMDs than NIRCam.

3.5. WLM

WLM (Wolf 1909; Melotte 1926) is a metal-poor ([Fe/H] = −1.2; Leaman et al. 2009) star-forming dwarf galaxy at ~0.9 Mpc (e.g., Albers et al. 2019). Though slightly closer objects of this class exist (e.g., IC 1613), WLM is the nearest example of a low-metallicity environment in which resolved CO clouds have been detected (Rubio et al. 2015). It has a sufficiently high star formation rate in the past several gigayears that it should host a sizable population of AGB stars (e.g., Dolphin 2000; Weisz et al. 2014a; McQuinn et al. 2017a;

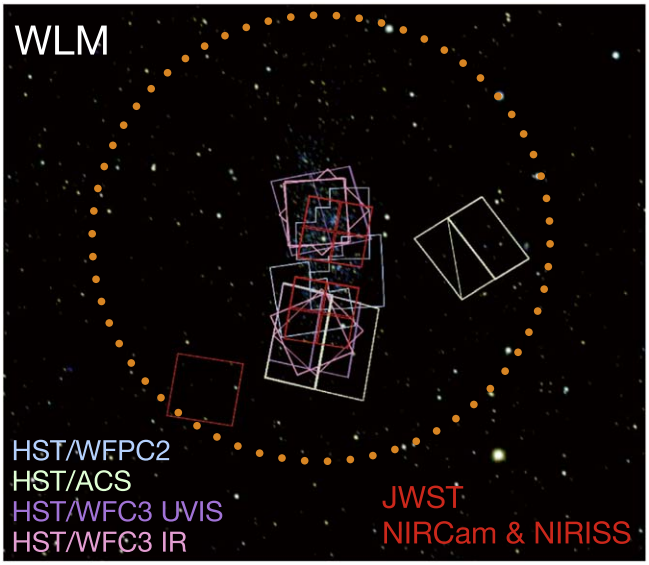

Figure 2. The locations of our NIRcam and NIRISS observations (plotted in red) for WLM overplotted on a Pan-STARRS optical image. The orange dotted lines indicates 1 r_h. An exhaustive, though not complete set of HST observations including HST/WFPC2 UV and optical imaging in blue (HST-GO-11079; Bianchi et al. 2012), HST/WFC3 UVIS UV imaging in purple (HST-GO-15275, PI: Gilbert), HST/ACS and HST/UVIS optical imaging in green (HST-GO-13768, PI: Weisz; Albers et al. 2019), and HST/WFC3 IR imaging in pink (HST-GO-16162, PI: Boyer). We opted not to undertake large dithers to fill the NIRCam chip and module gaps which would have substantially increased the program time while only marginally enhancing our science goals.

Albers et al. 2019). In terms of science, our JWST imaging of WLM will allow us to measure its SFH from the ancient MSTO and compare it to the existing HST-based SFH, measure its bulk PM using archival HST imaging, explore the stellar populations associated with its CO clouds, and construct parsec-scale extinction using IR-only techniques and combined UV–optical–IR HST and JWST stellar SEDs (e.g., Dalcanton et al. 2015; Gordon et al. 2016). On the technical side, our observations of WLM allow us to test DOLPHOT in a regime of faint, crowded stars that is typical of more distant systems, and also test its capabilities for simultaneously measuring stellar photometry across facilities (HST and JWST) and instruments (WFPC2, ACS, UVIS, and NIRCam).

We required that one module of the NIRCam observations overlap UV–optical–IR HST observations as well as Atacama Large Millimeter/submillimeter Array (ALMA)-detected CO clouds (Rubio et al. 2015). As shown in Figure 2, the other NIRCam module overlaps with the deep optical HST/ACS imaging presented in Albers et al. (2019). We enforced this configuration by requiring orientations of 70°–110° or 250°–290°. This orientation placed the NIRISS field in the stellar halo of WLM, providing an expansion on the areal coverage to build on the population gradient studies of WLM (e.g., Leaman et al. 2013; Albers et al. 2019). We used ASTs associated with the deep HST imaging of Albers et al. (2019) to ensure that our NIRCam observations would only be modestly affected by stellar crowding.

We selected the F090W, F150W, F250M, and F430M filters for our NIRCam imaging of WLM. As discussed in Section 3.3, the SW filter combination F090W − F150W is likely to be widely used for SFHs measured from the ancient MSTO. Medium-band filters in the near-IR have proven remarkably efficient for the photometric identification and classification of AGB stars (e.g., Boyer et al. 2017). Our simulations, based on these studies, suggest that the F250M and F430M filters should work well for similar science. For NIRISS, we selected the F090W and F150W filters.

In the optical, measuring a well-constrained SFH for distant dwarf galaxies requires a CMD that reaches an S/N ∼ 5–10 at the oldest MSTO (e.g., Cole et al. 2007; Monelli et al. 2010; Cole et al. 2014; Skillman et al. 2014; Gallart et al. 2015; Skillman et al. 2017; Albers et al. 2019). Using MIST stellar models, we find that the ancient MSTO for metal-poor stellar population has $M_{\rm F090W} = +3.4$ and $M_{\rm F150W} = +3.1$. Using the parameters for WLM in Table 1 and v1.1.1 of the ETC, we estimated that 33,241 s in F090W and 18,724 s in F150W would reach the required depths of $m_{\rm F090W} = 28.3$ and $m_{\rm F150W} = 28.1$ with an S/N = 10 in each filter.

3.6. Program Updates since 2017

Our program has only had minor changes since it was first approved in 2017 November. In 2021, we changed the DEEP2 readout patterns for WLM and Draco II to MEDIUM8, following updated advice from a STScI technical review. The number of groups and integrations was changed accordingly. In 2021, STScI increased our allocated time from 27.35 to 27.5 hr to reflect updated overhead accounting.

Following commissioning in spring 2022, STScI staff changed the range of aperture PA ranges of Draco II from unconstrained to be have a value of 47°–118°, 143°–280°, or 354°–24° in order to avoid the "claws" feature,[35] which is due to stray light from a bright source that is outside the field of view of NIRCam (STScI 2016; Rigby et al. 2023).

4. Observations

We acquired NIRCam and NIRISS imaging of our three targets in 2022 July and August. Figure 1 and Figure 2 show the NIRCam and NIRISS footprints for each of our targets overlaid on ground-based images and Table 1 lists our observational configurations. Full details on implementation can be viewed by retrieving proposal 1334 in the APT.[36]

We followed the same fundamental observing strategy for all three targets. For each target, the primary instrument, NIRCam, imaged a single central field in the SW and LW filters as described in Section 4. NIRISS obtained imaging in parallel in the two filters F090W and F150W.

All observations were taken with the four point subpixel dither pattern `4-POINT-MEDIUM-WITH-NIRISS`. This pattern ensured adequate PSF sampling for both cameras, as well as improved rejection of cosmic rays, hot pixels, etc.

We opted against primary dithers. The main advantage of the primary dithers is to fill the gaps between the detectors and/or modules. However, the intergap imaging is generally shallower than the rest of the data and requires more JWST time to acquire. For our particular science cases, including primary dithers added a modest amount of time to the program but would not substantially enhance the data for our main science goals. Other science cases (e.g., covering a large region such as PHAT did) may benefit from primary dithers and filling gaps.

[35] https://jwst-docs.stsci.edu/jwst-near-infrared-camera/nircam-instrument-features-and-caveats/nircam-claws-and-wisps
[36] https://apt.stsci.edu

For M92, we used the SHALLOW4 readout pattern for NIRCam and the NIS readout pattern for NIRISS. The orientation was constrained to an aperture PA range of 156° to 226° in order to maximize the possibility of overlap between the NIRISS field and existing HST imaging, while also allowing for reasonable schedulability very early in the lifetime of JWST. The central location of the NIRCam field ensures it will overlap with existing HST imaging. Including overheads, the total time charged for observing M92 was 7037 s. The ratio of science-to-charged time was ∼0.35 (counting the primary NIRCam imaging only) or ∼0.7 (for both NIRCam and NIRISS imaging). The data volume was well within the allowable range. After performing photometry (Section 5), we found that the third exposure of M92 exhibited much worse astrometric alignment than other three exposures. Because 100% of the data were acquired before we could determine if this alignment was due to the observations themselves (i.e., as opposed to an issue with our software, the JWST pipeline), we were unable to request a WOPR due to the 90% rule that governs reobservations. We include this exposure in the present paper's photometry and briefly discuss it in Section 6.1.1.

For Draco II, we used the MEDIUM8 readout pattern for NIRCam and the NIS readout pattern for NIRISS. The NIRCam field was centered on the galaxy and will largely overlap with existing HST imaging and Keck spectroscopic data. The large angular separation of the NIRISS and NIRCam fields compared to the size of Draco II means that the NIRISS field will contain few, if any, bona fide members of Draco II. Including overheads, the total time for observing Draco II was 24,539 s. The ratio of science-to-charged time was ∼0.71 (counting the primary NIRCam imaging only) or ∼1.36 (for both NIRCam and NIRISS imaging). The data volume was well within the allowable range.

For WLM, we used the MEDIUM8 readout pattern for NIRCam and the NIS readout pattern for NIRISS. The NIRCam field was placed in the center of WLM in order to overlap the low-metallicity molecular clouds discovered by ALMA as well as deep archival optical HST imaging. Subsequent UV and near-IR HST imaging of WLM obtained by members of our team were placed to maximize the chances of overlap with our JWST observations of WLM.

Including overheads, the total time charged for observing WLM was 66,884 s. The ratio of science-to-charged time was ∼0.8 (counting the primary NIRCam imaging only) or ∼1.50 (for both NIRCam and NIRISS imaging). The large data volume (19.962 GB) for WLM generated a "Data Excess over Lower Threshold" warning in APT. Though this level of warning is only a recommendation to mitigate data volume excess, we nevertheless consulted with STScI about mitigation strategies. However, we were unable to identify a way to reduce data volume without compromising the science goals and no changes were made. We caution that even longer integrations (e.g., that may be needed for deep CMDs outside the LG) may require careful planning to avoid data volume limitations.

Because our WLM observations span several continuous hours (Table 2), our observations of WLM should allow us to recover the light curves of short period variables (e.g., RR Lyrae). Generation of the light curves requires performing photometry on calibrated images at each integration. At the time of this paper's writing, due to the large data volume, the STScI JWST reduction pipeline generates integration-level calibrated images only when the time series observation (TSO) mode is used. However, we were unable to use the TSO mode of JWST as it does not permit dithers nor parallel observations. Instead, producing the necessary images to generate light curves requires running the reduction pipeline locally and creating custom time series analysis software, which is beyond the scope of this paper.

In total, all of our science observations with NIRCam total 20.45 hr and observations with NIRISS total 17.85 hr, indicating a fairly high ratio of science-to-charged time.

Figures 3, 4, and 5 show false color images of each NIRCam field. M92 and WLM have zoom-ins of select regions inset to illustrate the exquisite detail of resolved nearby systems afforded by JWST.

5. Photometry

We perform photometric reductions of our observations using the newly developed NIRCam module for DOLPHOT. The detailed description of how DOLPHOT works is well documented in the literature (e.g., Dolphin 2000; Dalcanton et al. 2012b; Dolphin 2016) and the functionality of the new NIRCam module is summarized in Section 2.2. A more detailed write-up of the DOLPHOT NIRCam and NIRISS modules are the subjects of an upcoming paper from our team. For this paper, we only focus on the NIRCam data. The WebbPSF[37] NIRISS PSF models appear to concentrate light significantly more than what we have observed in the ERS images. Consequently, our NIRISS photometry is not yet reliable and further updates await improvements to the PSF models. NIRCam suffers from a similar issue, but to a much smaller degree.

We first acquired all images from MAST (the specific observations used in his paper can be accessed via doi:10.17909/71kb-ga31). Per their FITS headers, versions of all JWST images used in this paper have the following JWST pipeline version information: CAL_VER = 1.93.2, CRDS_VER = 11.16.18, and CRDS_CTX = jwst_p1063.pmap. Next, we performed DOLPHOT reductions on the level 2b crf frames and use the level 3 i2d F150W drizzled image as the astrometric reference frame. The use of this reference image ensures excellent internal alignment of our image stack and ties the absolute astrometry to Gaia DR2. We perform photometry in all four bands simultaneously. Since there is no spatial overlap between the footprints of the two NIRCam modules, we photometer them independently and merge the catalogs a posteriori.

We have not included Frame 0 in the photometric reductions for this paper. As of this paper's writing, the JWST pipeline does not automatically provide Frame 0, requiring these images be generated locally. Even when created with our own execution of the JWST pipeline, we have yet to resolve fully how the $1/f$ noise issue (e.g., Schlawin et al. 2020; Bagley et al. 2023) can be resolved in a manner that ensures self-consistent photometry with DOLPHOT for all frames. This issue will be addressed in more detail in our forthcoming photometry paper. In the meantime, without Frame 0 data, our photometry saturates at fainter magnitudes that we expect to recover once the Frame 0 data are included in our DOLPHOT runs.

For our photometric reductions, we adopt the DOLPHOT parameter setup recommended by PHAT (Williams et al. 2014).

[37] https://webbpsf.readthedocs.io/en/latest/

Table 2
A Summary of Our JWST ERS Observations Taken in 2022

Target	Date	Camera	Filter	t_{exp} (s)	Groups	Integrations	Dithers
M92	June 20–21	NIRCam	F090W/F277W	1245.465	6	1	4
		NIRCam	F150W/F444W	1245.465	6	1	4
		NIRISS	F090W	1245.465	7	1	4
		NIRISS	F150W	1245.465	7	1	4
Draco II	July 3	NIRCam	F090W/F480M	11,810.447	7	4	4
		NIRCam	F150W/F360M	5883.75	7	2	4
		NIRISS	F090W	11,123.294	9	7	4
		NIRISS	F150W	5883.75	10	3	4
WLM	July 23–24	NIRCam	F090W/F430M	30,492.427	8	9	4
		NIRCam	F150W/F250M	23,706.788	8	7	4
		NIRISS	F090W	26,670.137	17	9	4
		NIRISS	F150W	19,841.551	19	6	4

We use the parameters recommend for ACS from PHAT for the SW images and the WFC3/IR parameters for the LW images. Subsequent data releases will make use of a set of parameters that we are tailoring to NIRCam and NIRISS observations of resolved stars.

We make use of NIRCam PSF models generated with WebbPSF v1.0.1 (Perrin et al. 2014). We use the optical path delay maps from 2022 July 24 (the best-matching file to our WLM observation epoch). Inspection of JWST's wave front field at the epochs of our three observations show little variation in the optical performance of the telescope, justifying our choice of a common PSF library. We are currently working in quantifying the full effect of JWST time-dependent PSF variations on DOLPHOT photometry.

The final products of the DOLPHOT photometric run are catalogs with positions, VEGAmag magnitudes (calibrated using the latest NIRCam zero-points[38]), uncertainties based on photon noise, and a set of quality metrics related to the goodness of point-source photometry (e.g., S/N, χ^2 of the PSF fit, angular extent of the source, and crowding level). At this stage, metrics such as the photometric error and the S/N are based on a Poissonian treatment of photon noise. While in many cases this is sufficient for a rough estimation, there are caveats associated with this approximation, especially when measuring stars in very crowded fields, or close to the limiting magnitude. We will provide a more thorough discussion on S/N estimation in our upcoming JWST DOLPHOT photometry paper.

The catalogs provided by DOLPHOT are subsequently inspected and culled to remove contaminants (e.g., artifacts, cosmic rays, and extended sources) while aiming to retain the largest number of bona fide stars. We identify a set of quality-metric cuts, listed in Table 3, which provide a reasonable trade-off between completeness and purity of the stellar sample; though for this initial presentation we erred on the side of purity. The selection criteria need to be satisfied in the F090W and F150W bands simultaneously. We only use the SW bands as they are shared by all three targets, allowing a common set of culling criteria. Our initial exploration suggests that the LW photometry may improve star–galaxy separation at faint magnitudes. This important topic is being further investigated by members of our team.

[38] https://jwst-docs.stsci.edu/jwst-near-infrared-camera/nircam-performance/nircam-absolute-flux-calibration-and-zero-points

Full characterization of uncertainties in resolved stellar populations studies required ASTs. ASTs consist of adding mock stars of known properties into each frame and recovering them using the same photometric procedure that is applied to the real data. For the purposes of this paper, i.e., focused on a survey description, we have not included the results of the ASTs. The large data volume and multifilter nature of the data make running ASTs computationally challenging. We will present full AST results and analyses in the upcoming JWST DOLPHOT photometry paper.

6. Discussion

6.1. CMDs

Figure 6 shows NIRCam SW CMDs for all three targets over the same magnitude range. The juxtaposition of these CMDs illustrates the quality and diversity of science possibilities provided by our program. In each panel, we overplot select S/Ns reported by DOLPHOT. As discussed in Section 5, these S/Ns are solely based on photon noise and do not account for the effects of crowding and incompleteness. We discuss the S/Ns further in Section 6.2.

The S/N for each target is remarkable, with S/Ns ranging from 500 near the MS kink to 10 for the lowest-mass stars in M92 and Draco II. WLM has a photon-noise-based S/N of ∼50 at the oldest MSTO, making it the highest-fidelity resolved star observation of a distant dwarf in existence. We now discuss the multiband CMDs for each of our targets in more detail.

Figures 7–9 show illustrative NIRCam CMDs in a selection of filter combinations for each ERS target. In all cases, we apply the catalog culling parameters described in Section 5 and listed in Table 3.

For guidance, we overplot a selection of stellar isochrones from the PARSEC v1.2S stellar libraries (Bressan et al. 2012; Chen et al. 2015). These models span the full range of metallicities and ages needed to characterize our data sets. We have adjusted these isochrones to the distances and reddenings listed in Table 1.

6.1.1. M92

Figure 7 shows select NIRCam CMDs for M92, along with select HST-based CMDs for comparison. The HST CMDs were reduced using DOLPHOT and the parameters recommended in Williams et al. (2014).

We overplot select PARSEC isochrones at a fixed age of 13 Gyr with varying metallicities, which we discuss below.

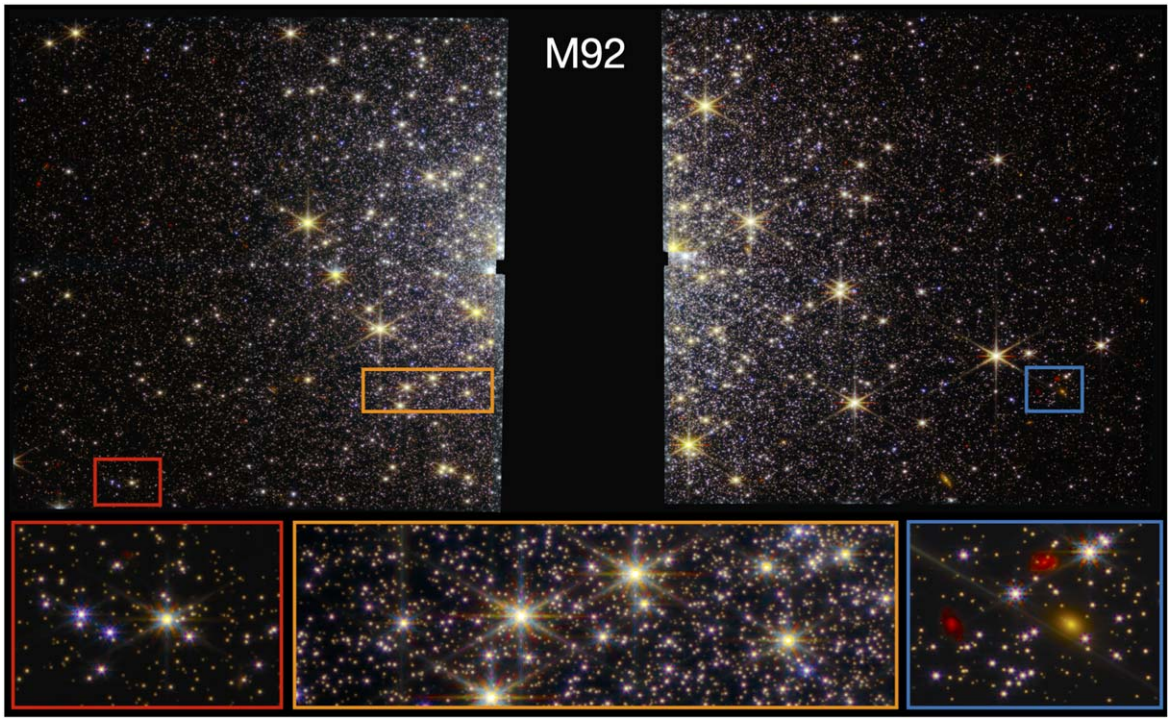

Figure 3. NIRCam color composite of M92. F090W was used as the blue channel, F150W as the green, and a combination of the two LW filters (F277W and F444W) as the red channel. The red and orange boxes highlight the stellar densities at $\sim 1\ r_h$ and $\sim 0.5\ r_h$. The blue box shows the presence of member stars as well as prominent background galaxies (red and yellow extended sources). The central black bar is the intermodule gap, over which we opted not to dither.

Though stars brighter than F090W ~ 18 are omitted due to saturation effects (see Section 5), key CMD features for faint, low-mass stars are clearly visible. Notably, the MS kink, which is due to opacity effects in M dwarfs, the region in which is in panels (a)–(c) at F090W ~ 21 and F150W ~ 20. The MS kink exhibits the sharpest inflection point in the F150W − F277W filter combination. The kink is much less pronounced in the F277W − F444W CMD (panel (d)). This is partially due to the lower S/Ns of the LW observations as well as the LW filters being far into the Rayleigh–Jeans tail of the stars' SEDs, which makes them only weakly sensitive to stellar temperature, thus resulting in similar colors and a less obvious kink.

Our NIRCam observations have produced the deepest CMD of M92 to date. The data extend fainter than the lowest stellar mass ($0.09\ M_\odot$) available from the standard PARSEC stellar library in the SW filters and to slightly higher masses ($0.12\ M_\odot$) in the LW filters.

The faintest objects in the F090W − F150W CMD fall into the bright end of the expected hydrogen-burning sequence. The exact mass at which a star-like object cannot sustain hydrogen fusion has long been debated (e.g., Hayashi & Nakano 1963; Kumar 1963; Chabrier et al. 2000). For this analysis, we computed custom PARSEC models with a mass resolution of $0.002\ M_\odot$ and find that that the minimum mass for hydrogen burning is $0.078 \leqslant M < 0.08\ M_\odot$ for a metallicity of [Fe/H] $= -1.7$ dex and an age of 13 Gyr. This translates to a magnitude range of $28.2 < m_{\rm F090W} \leqslant 29.5$ mag in M92. This depth is quite remarkable considering our observations only consist of $\sim$1050 s in each filter. In comparison, the faintest stars in the HST WFC3/IR CMD (panel (e)) are a few magnitudes brighter despite $\sim$1200 s of integration time in each filter. To date, comparably deep IR studies of metal-poor, extremely low-mass stars with HST have been limited to the nearest GCs (e.g., M4; Dieball et al. 2016, 2019). As our M92 data show, the superior sensitivity of NIRCam will make such studies possible throughout the MW.

The PARSEC models overplotted in Figure 7 are nominally higher than the metallicity of M92 ([Fe/H] $= -2.23$ dex) derived from high-resolution APOGEE spectroscopy (Mészáros et al. 2020). This discrepancy is because the current version of the PARSEC models are solar scaled, whereas M92 is highly α-enhanced with $[\alpha/{\rm Fe}] \sim 0.5$ dex. Well-established corrections can be applied to match solar-scaled models with α-enhanced populations (e.g., Salaris et al. 1993). For M92, the corrective factor for the PARSEC models results in values of [Fe/H] $\sim$ 0.5 dex higher than derived from spectroscopy. PARSEC models with α-enhancements are under construction and will mitigate the need to apply such corrections.

Overall, the PARSEC models are in reasonably good agreement with the NIRCam CMDs. For the F150W − F444W and F277W − F444W CMDs, the models trace the loci of the data quite well. However, for the F090W − F150W and F150W − F277W CMDs, the models are systematically too blue by $\sim$0.05 mag. The source of this offset is not due to distance, reddening, age, or metallicity as these same models are well matched to the MSTO in the brighter HST CMDs (Figures 7(e) and (f)). In general, stars above the MS kink are well matched by the models in the LW NIRCam and HST filters, limiting the offsets to only SWs. One possible source of the offset is the presence of poorly modeled absorption features (e.g., TiO) in the atmospheres of very cool, low-mass stars. A detailed exploration of this offset is beyond the scope of this paper, but we note that deep JWST imaging of a larger set of GCs in several filters has the potential to help elucidate the exact nature of this issue.

The NIRCam CMDs also exhibit scatter in color that is larger than photon noise and variations in age or metallicity. One possible physical explanation is the presence of multiple

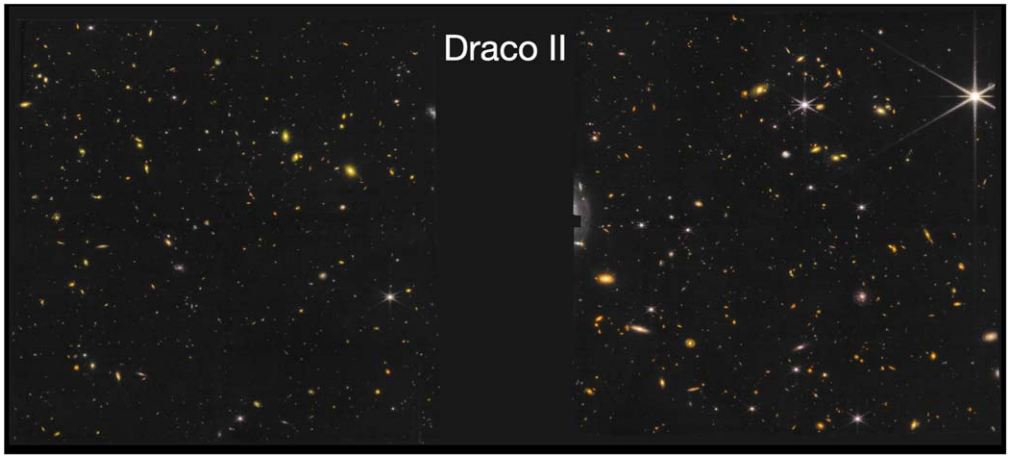

Figure 4. NIRCam color composite of Draco II. F090W was used as the blue channel, F150W as the green, and a combination of the two LW filters (F360M and F480M) as the red channel. The central black bar is the intermodule gap, over which we opted not to dither. The stellar density of Draco II is so low that background galaxies by far dominate the image. Only software like DOLPHOT is able to locate the faint stars that are members of Draco II.

chemically distinct populations. Like many luminous Galactic GCs, M92 exhibits multiple populations with distinct abundance patterns (e.g., Mészáros et al. 2020). Other GCs with deep CMDs and similar abundance patterns show a broadening of stellar sequences at and below the MS kink. This broadening has been attributed to the persistence of these chemically distinct sequences to the lowest stellar masses (e.g., Milone et al. 2012, 2014; Correnti et al. 2016; Milone et al. 2017), which is thought to be driven by oxygen variations expressed via water lines (e.g., Dotter et al. 2015; VandenBerg et al. 2022; Ziliotto et al. 2023).

Finally, we note that at this early stage in the lifetime of JWST it is clear from our photometry of M92 that there are still zero-point offsets between the different chips. This is most obvious in Figure 7(d) in which a bifurcated CMD is clearly visible. The color difference is F277W − F444W $\sim$ 0.1 mag. We found that the two MS populations each correspond to a different LW module, with the bluer population from LW module A and the redder population from LW module B. The broadness of the SW – LW CMDs in panels (b) and (c) are also due to zero-point offsets, with the largest contributions from the LW modules. The SW channels also show some flux offsets among chips at the $\sim$0.02 mag level. Notably SW modules B1 and B2 appear to be slightly bluer than the other chips. Some of the scatter in all of the CMDs is due to the comparatively poor astrometric alignment of the third M92 exposure. We will undertake a more detailed exploration of the offsets and effects of the third exposure in the upcoming photometry paper. Finally, as discussed in Gordon et al. (2022), the flux calibration of JWST is ongoing and it is expected that the offsets we currently find will become negligible as new flux calibrations are made available.

6.1.2. Draco II

Figure 8 shows select NIRcam CMDs of Draco II, along with the deepest existing optical HST CMD for reference (GO-14734; PI: N. Kallivayalil). Like M92, the brightest stars in Draco II suffer from saturation and are not included in our current photometric reduction. We include the same PARSEC isochrones as shown in M92 (Figure 7) as Draco II hosts a comparably ancient (13 Gyr), metal-poor, and likely α-enhanced stellar population (e.g., Longeard et al. 2018; Simon 2019). The selected isochrones provide a good fit to the MSTO in the HST CMD (panel (b)) suggesting the adopted parameters (i.e., age, metallicity, distance, and extinction) are reasonable, but as with M92, the models are slightly too blue in the NIRCam SW CMDs of Draco II.

Our F090W − F150W CMD of Draco II is the deepest CMD of a galaxy outside the MW and has imaged the lowest-mass stars outside the MW (0.09 $M_{\odot}$).

Previously, the deepest CMD in an external galaxy was from Gennaro et al. (2018b), who used HST WFC3/IR data of MW UFD Coma Berenicies to study its low-mass IMF. From 32,780 s of integration time in each filter, their F110W and F160W photometry reached a usable low-mass limit of 0.17 $M_{\odot}$, whereas our data extend to 0.09 $M_{\odot}$. The large dynamic range of stellar masses in Draco II provides excellent leverage for a low-mass IMF measurement. Tight constraints on the IMF in Draco II could provide a new means of distinguishing whether faint stellar systems are dark-matter-dominated dwarf galaxies or GCs (e.g., Willman & Strader 2012; Baumgardt et al. 2022), as well as insight into star formation in extreme environments (e.g., Geha et al. 2013; Krumholz et al. 2019).

The width of the lower MS is in excess of the photometric noise. Metallicities derived from the more-luminous stars in Draco II suggest a spread of $\sigma \sim 0.5$ dex (e.g., Li et al. 2017; Longeard et al. 2018; Fu et al. 2022), which may contribute to this scatter. Background galaxies are also a source of contamination and likely contribute to the scatter, particularly at the faintest magnitudes. The combination of very deep imaging and the sparsity of Draco II's stellar population mean that background galaxies are a large source of contamination. Our preliminary investigations indicate that the multicolor NIRCam photometry may be efficient for star–galaxy separation (J. T. Warfield et al. 2023, in preparation).

The F150W − F360M CMD (panel (c)) extends to a comparably low stellar mass as the SW CMD, albeit at a lower S/N. The LW CMD (panel (d)) is much shallower, though the primary purpose of these filters is to explore their potential as photometric metallicity indicators akin to the calcium H and K filters being used in the optical (e.g., Starkenburg et al. 2017b; Longeard et al. 2018; Fu et al. 2022).

As with M92, the stellar isochrones provide a good qualitative match to the data. The shape and magnitude of the MS kink appears to track the data well. However, as

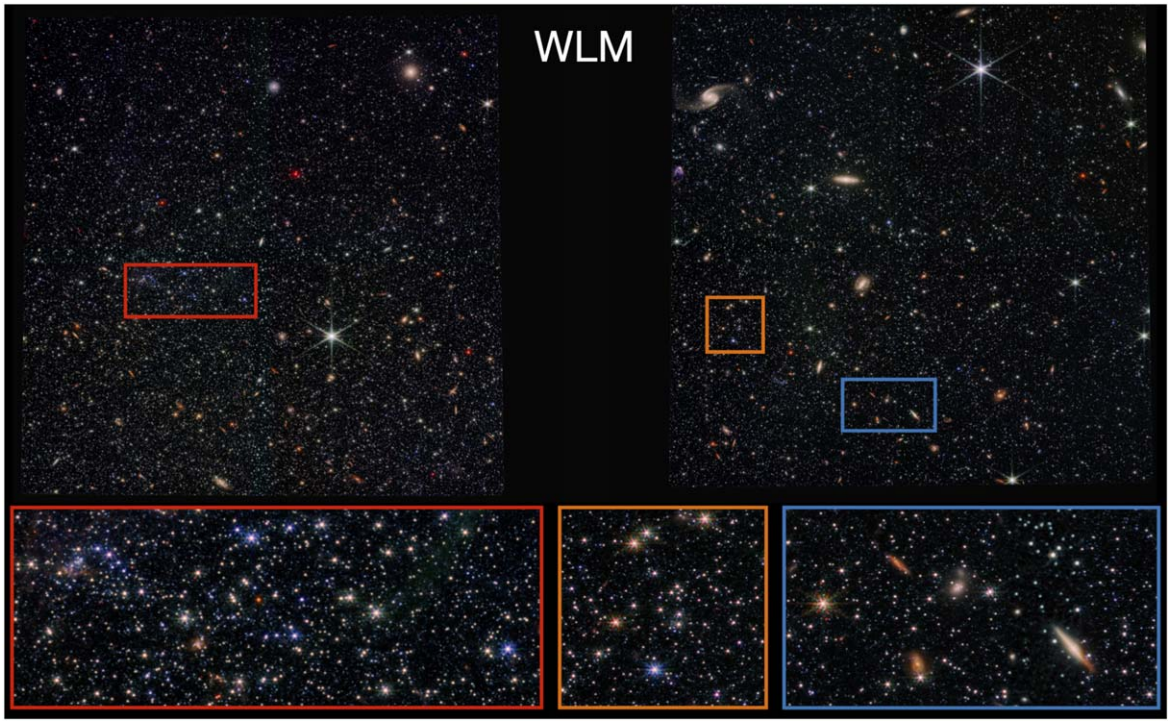

Figure 5. NIRCam color composite of WLM. F090W was used as the blue channel, F150W as the green, and a combination of the two LW filters (F250M and F430M) as the red channel. The red and orange boxes highlight the a young star-forming complex (red) and a more typical region (orange) in WLM. The blue box shows the presence of member stars as well as several background galaxies. The central black bar is the intermodule gap, over which we opted not to dither.

Table 3
Quality-metric Criteria Used to Cull Our DOLPHOT Photometric Catalogs

Band	S/N	Sharp^2	Crowd	Flag	Object Type
F090W	$\geqslant 4$	$\leqslant 0.01$	$\leqslant 0.5$	$\leqslant 2$	$\leqslant 1$
F150W	$\geqslant 4$	$\leqslant 0.01$	$\leqslant 0.5$	$\leqslant 2$	$\leqslant 1$

discussed in the context of M92 the models are modestly too blue compared to the data.

6.1.3. WLM

Figure 9 shows select NIRCam CMDs for WLM, along with the deepest optical CMD of WLM taken with HST. Due to its large distance, few stars in WLM are affected by saturation.

The CMDs of WLM exhibit a wide variety of stellar sequences that span a range of ages and phases of evolution. Examples include the young MS, the RGB and AGB, the HB, and the oldest MSTO. The relative positions of these features are generally similar to what is known for optical CMDs with subtle changes due to the shift to IR wavelengths (e.g., Dalcanton et al. 2012a; Williams et al. 2014; Gull et al. 2022). For example, the HB slopes to fainter values at bluer wavelengths as hot blue HB stars are less luminous at IR wavelengths. Similarly, red stars (e.g., RGB and AGB) become more luminous as the IR wavelengths are closer to their peak temperatures compared to optical wavelengths.

Figure 9 shows that our NIRCam SW CMD of WLM is at $\sim$1 mag deeper than the HST/ACS CMD despite similar integration times ($\sim$54,200 s for NIRCam versus $\sim$61,400 s for ACS). This increase owes primarily to the increased sensitivity of JWST at these wavelengths. K. B. W. McQuinn et al. (2023, in preparation) is deriving the SFHs from both data sets to quantify the capabilities of JWST imaging for detailed SFH determinations.

More broadly, our CMDs of WLM are the deepest in existence for an isolated dwarf galaxy. Prior to our program, HST/ACS observations of Leo A from Cole et al. (2007) extended to the lowest stellar masses in a galaxy outside the immediate vicinity of the MW. The HST observations of Leo A reach nearly as deep, but the larger distance of WLM (0.5 mag farther) means that our measurements actually extend to less-luminous stars on the MS.

Though not as deep as the SW data, the LW is remarkably deep for medium bands. The F090W − F250M data extend below the oldest MSTO, making it the deepest medium-band data available for an isolated dwarf galaxy. The F250M − F430M (panel (d)) CMD extends well below the red clump. These data are expected to provide an excellent means of identifying AGB stars and helping constrain their underlying physics.

The overplotted isochrones provide a reasonable match to the data. In this case, we have selected a single metallicity of $[\mathrm{Fe/H}] = -1.2$ dex matched to RGB spectroscopic abundances (Leaman et al. 2009), and plotted select ages that range from 50 Myr to 13 Gyr. Visually, the PARSEC models provide a good qualitative match to the data. The level of agreement will be formally quantified in K. B. W. McQuinn et al. (2023, in preparation). We note that, as with M92, there is some degree of flux offset between the two LW modules in WLM that causes a color shift of F250M − F430M $\sim$ 0.05 mag. We detailed this more in the upcoming photometry paper and expect improvement in the relative flux zero-points between the modules as the JWST calibration program progresses (Gordon et al. 2022).

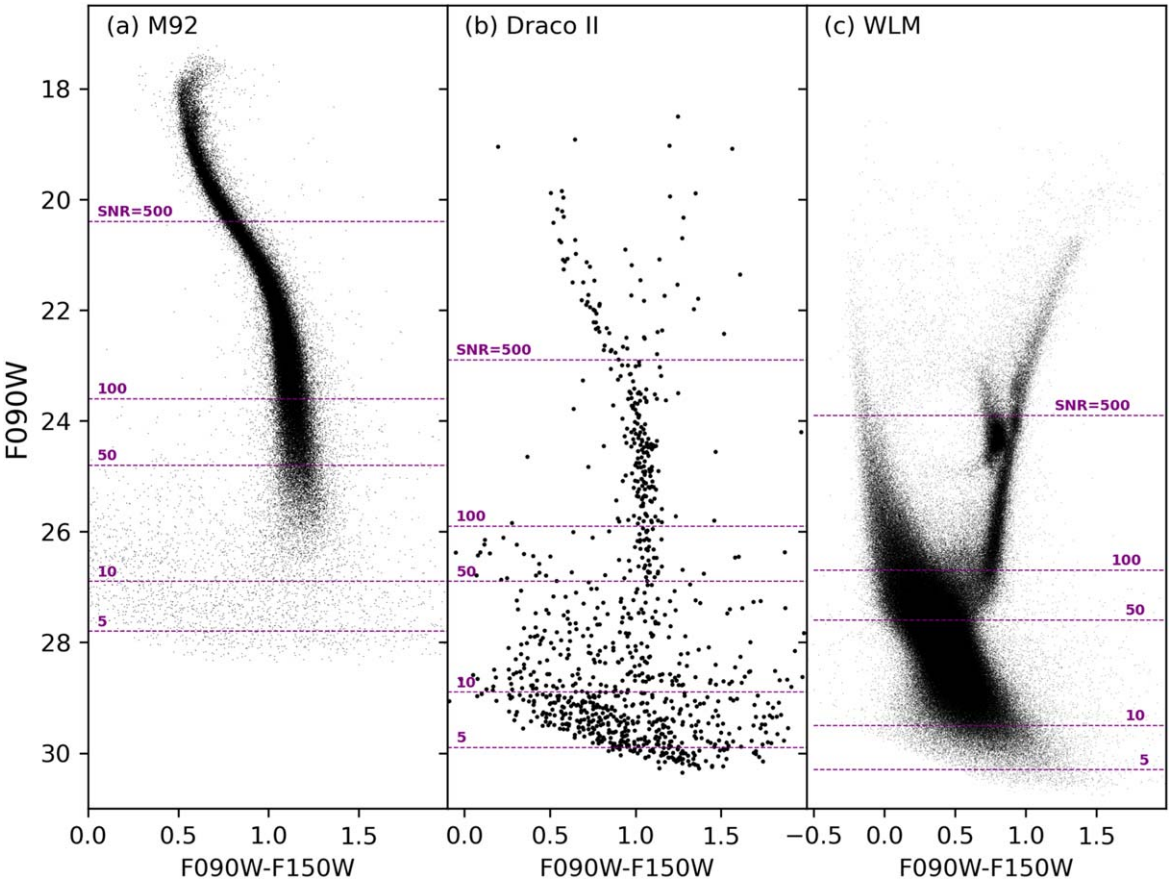

Figure 6. CMDs from all eight NIRCam chips for each of our targets. (a) M92 extends from our bright saturation limit without Frame 0 data (F090W $\sim$ 18) near the MSTO and reaches just fainter than the hydrogen-burning limit (F090W $>$ 28.2). The inflection point of the MS at F090W $\sim$ 21 is the MS kink. (b) The CMD of Draco II includes the MS kink at F090W $\sim$ 23 and reaches the bottom of the stellar sequence provided by the standard PARSEC models (0.09 $M_{\odot}$). (c) The CMD of WLM displays a wide variety of stellar sequences that span a range of ages including young stars (e.g., the upper MS and red core helium burning stars), intermediate-age stars (e.g., AGB and RGB stars), and ancient stars that span a wide range of colors and magnitude (e.g., RGB, SGB, MSTO, and lower MS). This CMD of WLM (S/N = 10 at $M_{\rm F090W} = +4.6$) is the deepest taken for a galaxy outside the immediate vicinity of the MW.

6.2. Comparisons with the ETC

Our photometry provides an opportunity to gauge the accuracy of the NIRCam ETC in practice.

In Figure 10, we consider the S/Ns for stars in M92 as reported by DOLPHOT against what is reported by the NIRCam ETC. M92 is the best of our three targets for this exploratory exercise as it is not particularly crowded and its CMD is well populated. The lack of crowding means that the S/Ns reported by DOLPHOT are a reasonable proxy for real noise, whereas the ASTs are necessary to assess the noise accurately in even moderately crowded images.

We compute the S/N as a function of F090W and F150W by only considering stars that pass a stricter version of the culling criteria listed in Section 5. Specifically, we require that each star has *crowd* $\leqslant$0.1, which eliminates all but the least-crowded stars. We also only consider stars with $0.2 < \mathrm{F090W} - \mathrm{F150W} < 1.5$, which isolates the MS in the SW filters and removes much of the contamination (e.g., background galaxies and diffraction spike artifacts) from our analysis. Finally, we exclude the brightest stars as they may be affected by (partial) saturation. We specifically only consider stars fainter than F090W = 20 and F150W = 19 for their respective S/N calculations.

From stars that pass these cuts, we compute the 50th, 16th, and 84th percentiles of the F090W and F150W S/N distributions in 0.25 mag bins over the entire magnitude ranges considered.

For the expected S/Ns, we use v2.0 of the JWST ETC to compute the S/N as a function of F090W and F150W magnitude. In the ETC, the detector strategies are set to match our F090W and F150W observational setup for M92 as listed in Table 2 and described in Section 3.3. We verified that the integration times in the ETC are identical to what our program acquired.

For the ETC scene, we used a K5V star ($T_{\rm eff} = 4250$ K and $\log(g) = 4.5$ dex) from the Phoenix stellar models. Though the stellar type varies over the color and luminosity ranges considered, we found that reasonable changes in the choice of stellar atmosphere only affected our findings at the $\sim$5% level. For simplicity, we adopted a single stellar atmosphere model for this calculation.

We adopted an extinction of $A_V = 0.06$ mag and an MW extinction curve. We set the background model to the central coordinates of M92 on 2022 June 20, the date of our observations. We computed the S/Ns in the F090W and F150W filters in 0.5 mag steps from 19 to 30 mag in each filter, renormalizing after extinction was applied.

The result is a smooth variation in S/N as a function of magnitude. We interpolated the results onto a finer magnitude grid for clearer comparison with the DOLPHOT results. Interpolation errors are $<$1%.

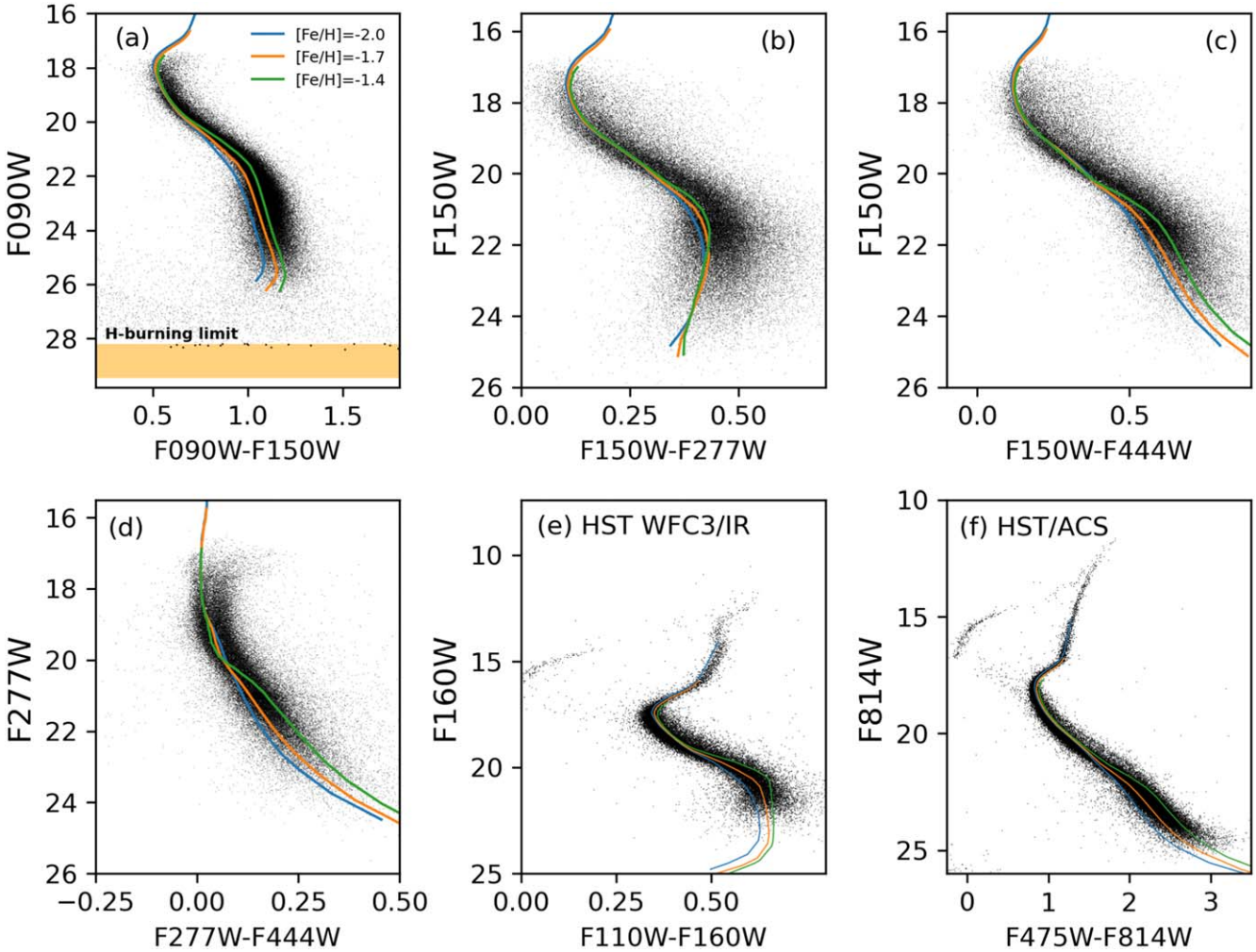

Figure 7. Select NIRCam CMDs of M92, along with HST WFC3/IR (HST-GO-11664) and ACS/WFC (GO-9453, GO-10775, GO-12116, and GO-16298) CMDS. Overplotted are solar-scaled PARSEC stellar models at a fixed age (13 Gyr) over a select range of [Fe/H] values, which have been corrected to match the known α-enhancement of M92 (Mészáros et al. 2020). The SW NIRCam CMD extends from our saturation limit (F090W $\sim$ 18) to below the lowest-mass star from the standard PARSEC models ($M = 0.09\ M_{\odot}$) and into the expected hydrogen-burning limit regime ($0.078 \leqslant M < 0.08\ M_{\odot}$). The LW CMDs reach slightly higher limits ($M = 0.12\ M_{\odot}$). These are among the deepest CMDs of a GC in existence and highlight how JWST will easily enable the study of prominent features for low-mass stars such as the MS kink and lowest-mass stars. The double MS in panel (d) and broadness of the CMDs in panels (b) and (c) are in part due to an 0.1 mag offset in the flux calibrations of LW modules A and B. While the stellar models are in excellent agreement with the more-luminous stellar evolutionary phases (e.g., RGB and MSTO) in the HST CMDs, they are $\sim$0.05 mag too blue for the lower-mass stars in the SW JWST filters. This offset could be due to the complex atmospheres of low-mass stars or the in-progress nature of the absolute flux calibrations.

To compute the S/Ns, we used the default aperture photometry setup in the NIRCam ETC. Specifically, this uses an aperture radius of 0.″1 and performs background subtraction using an annulus 0.″22–0.″4 from the source. For both F090W and F150W, this radius within the aperture radius range of 2–3$\times$ the PSF FWHM specified in JDOX,[39] as recommended by the JWST help desk. We will explore more filter S/Ns and variations in the ETC photometric setup in a future paper.

Figure 10 shows a comparison between the S/Ns reported by DOLPHOT (gray shaded regions) and the NIRCam ETC (black lines) as a function of F090W and F150W magnitude. The bottom panels show the ratios of the DOLPHOT and ETC S/Ns. Both visually and quantitatively, the expected ETCs agree quite well. For most of the magnitude ranges, the DOLPHOT and ETC S/Ns agree within $\sim$20%, which is within the bounds of our uncertainty range. The small structures in the residuals over this range are due to the finite numbers of real stars in each bin. There are some noticeable deviations from unity at bright magnitudes for both F090W and F150W. We believe that these may be due to saturation effects that might be mitigated by improved data quality masks and/or the use of Frame 0 data. Both will be explored in our forthcoming DOLPHOT NIRcam module paper. Similarly, the increased ratio at the faintest F150W magnitudes is not overly concerning as small variations in the PSF shape (Dolphin 2000) and the presence of nonstellar artifacts at the very bottom of the CMD can affect the photon-noise-based S/Ns. The uptick could also be caused by the removal of objects that do not meet our culling criteria; formally a correct calculation requires factoring in completeness as determined by the ASTs.

Overall, this comparison provides preliminary indications that v2.0 of the ETC provides reasonable S/N estimates for fairly uncrowded stars imaged with NIRCam. Of course, in

[39] https://jwst-docs.stsci.edu/jwst-near-infrared-camera/nircam-performance/nircam-point-spread-functions

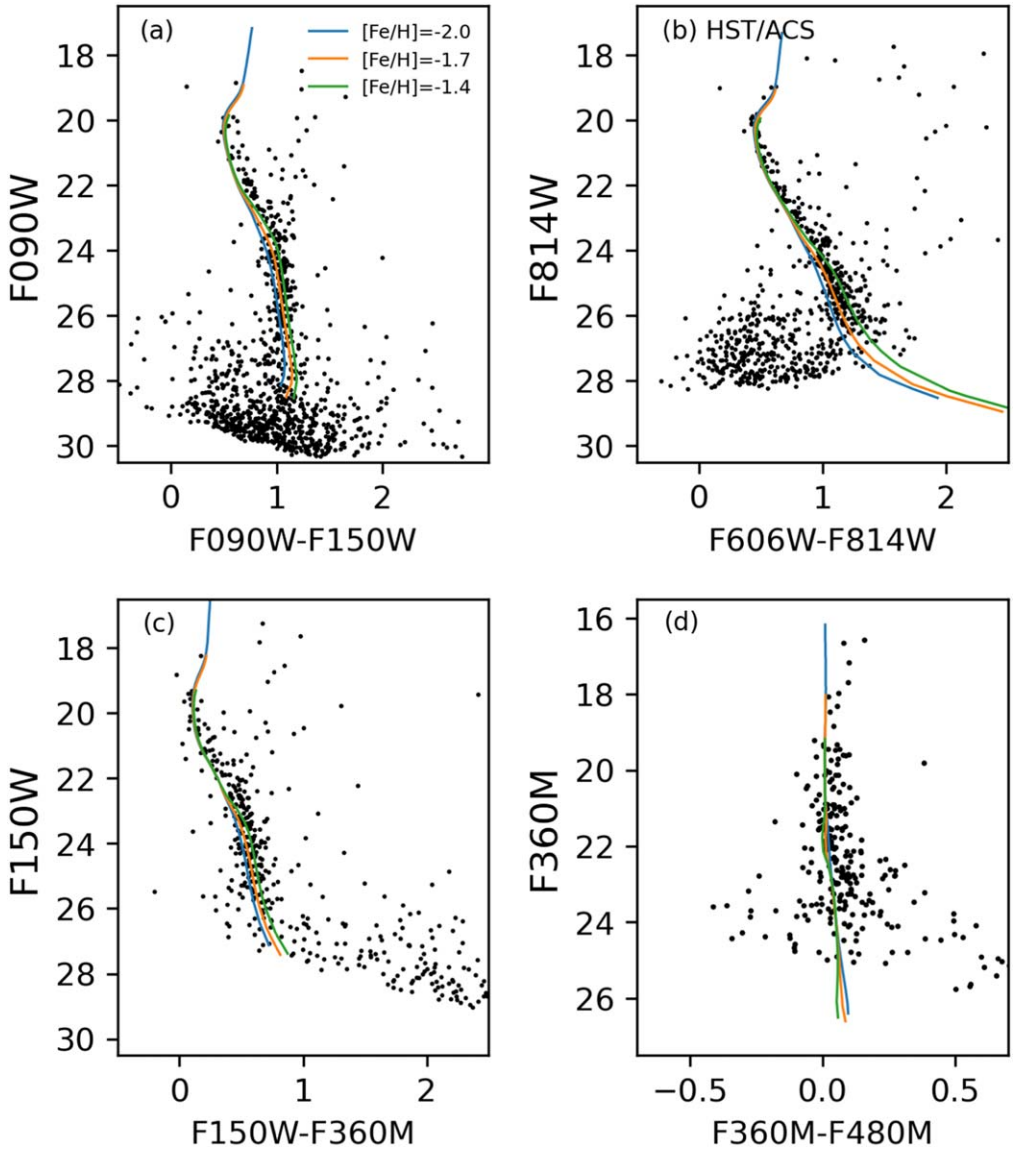

Figure 8. Select NIRCam CMDs of Draco II along with the deepest optical CMD which is based on HST/ACS imaging (GO-14734; panel (b)). Overplotted are PARSEC stellar models at a fixed age (13 Gyr) for the same [Fe/H] values selected for M92. The SW CMD extends to the lowest-mass stellar model ($M = 0.09\ M_{\odot}$), making it the deepest CMD of an MW satellite galaxy to date. The exquisite depth of our data indicates how JWST enables a variety of science, including constraining the low-mass IMF and quantifying low-mass star features (e.g,. the MS kink and objects near the hydrogen-burning limit) outside the MW.

practice, many resolved stellar systems that will be targeted by NIRCam will be more affected by crowding than M92, which can lead to larger discrepancies in the expected versus recovered S/N. For HST, this effect is partially mitigated by the optimal S/N reported by its ETC.[40] This number reflects the expected S/N for an isolated point source recovered by PSF fitting and is generally a factor of 1.5–2 higher than the regular S/N reported by the HST ETC. Our initial analysis of M92 suggests that the baseline S/Ns from the NIRCam ETC may not be off by as large a factor. However, further exploration is needed in a variety of images with variable crowding, stellar type, etc. Ultimately, the ASTs will aid in the calculation of the S/Ns seen in the data over a range of stellar densities. We will carry out such an exploration in the context of our NIRCam and NIRISS DOLPHOT photometry paper.

[40] https://etc.stsci.edu/etcstatic/users_guide/1_3_imaging.html

7. Summary

We have undertaken the JWST Resolved Stellar Populations ERS program in order to establish JWST as the premier facility for resolved stellar populations early in JWST's lifetime. In this paper, we have described the motivation, planning, implementation, execution, and presentation of NIRCam CMDs from preliminary photometric reductions with DOLPHOT. Some key takeaways from our survey include:

1. Our 27.5 hr program obtained NIRCam (primary) and NIRISS (parallel) imaging of three diverse targets: the Milky Way GC M92, satellite UFD Draco II, and the more distant (0.9 Mpc) star-forming galaxy, WLM. A summary of their properties are listed in Table 1 while a summary of our JWST observations for each target are listed in Table 2. These targets were selected in order to enable a variety of science and technical goals related to

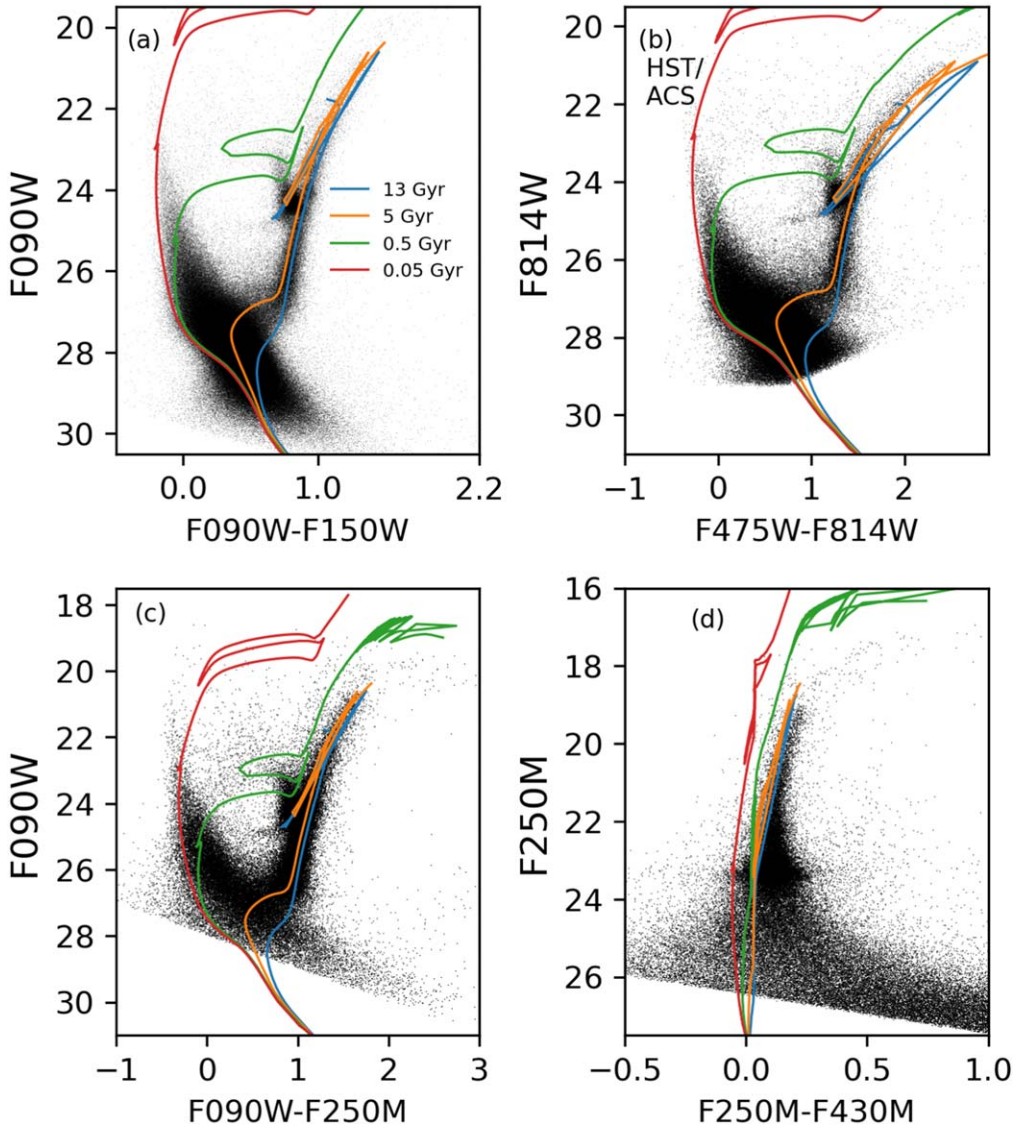

Figure 9. Select NIRCam CMDs of WLM along with the deepest available HST/ACS optical CMD from Albers et al. (2019). Overplotted are isochrones from the PARSEC solar-scaled stellar models at a fixed metallicity of [Fe/H] = −1.2 dex for a variety of indicated ages. Panel (a) is the deepest CMD of an isolated dwarf galaxy to date, extending ∼1.5 mag below the oldest MSTO; it is deeper than the HST CMD despite ∼7000 s less integration time. The isochrones indicate the variety of stellar ages present in WLM. The LW CMD shown in panel (d) extends ∼2 mag below the red clump. Such deep CMDs show that JWST will provide for a variety of science at different cosmic epochs including exquisite lifetime SFHs, the study of evolved red stars, TRGB distances, and very young stars in galaxies outside the LG.

resolved stellar populations analysis as described in Section 2.

2. This ERS program facilitated the development of NIRCam and NIRISS modules for DOLPHOT, a widely used stellar crowded field photometry package. We used our ERS targets to test these modules for a variety of image properties (e.g., various filter combinations, over a large dynamic range in stellar crowding). We describe the application of DOLPHOT to our ERS data in Section 5. Beta versions of these DOLPHOT modules, along with theoretical PSF models for all NIRCam and NIRISS filters are publicly available on our team website and on the DOLPHOT website.
3. We presented preliminary NIRCam CMDs in select SW and LW filter combinations from a first pass DOLPHOT reduction. The CMDs are among the deepest CMDs in existence for each class of object. The F090W − F150W CMD of M92 touches the hydrogen-burning limit (F090W > 28.2; $M < 0.08\ M_{\odot}$). The F090W − F150W CMD of Draco II reaches the the bottom of the stellar sequence ($0.09\,M_{\odot}$) in standard PARSEC models. The F090W − F150W CMD of WLM extends ∼1.5 mag below the oldest MSTOs in WLM.
4. We find that that flux offsets between the various detectors exist, most notably in the LW channels. This offset is most obvious in the M92 F277W − F444W CMD, in which two MS populations are presently offset by a color of 0.1 mag. We also identified color differences at the level of 0.02 mag in the F090W − F150W CMD and ∼0.05 mag in the F250W − F430M CMD of WLM. These color offsets contribute to the blurring or bifurcation seen in many of the CMDs. Continued progress in the JWST flux calibration program should lead to improvements.

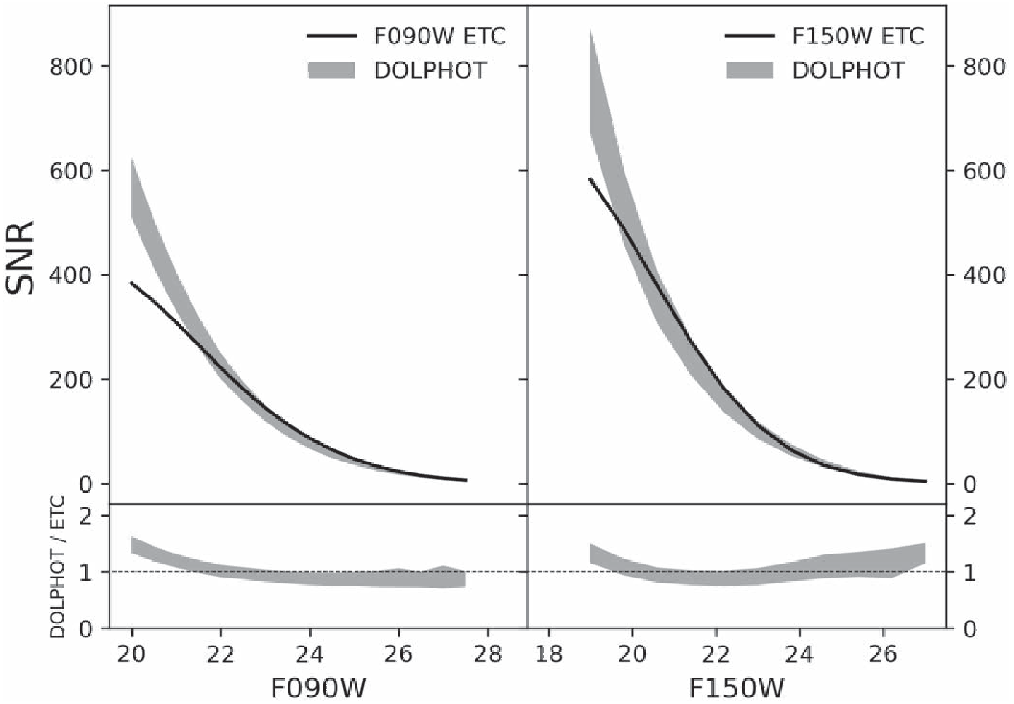

Figure 10. Comparisons between the photon-noise-based S/Ns from the DOLPHOT F090W and F150W photometry of M92 (gray shaded region) and the expected S/Ns from v2.0 of the NIRCam ETC (black lines). Over most of the dynamic ranges in magnitude the S/Ns reported by DOLPHOT and the ETC are consistent within the scatter (∼20%) of the data. Deviations at the bright end may be due to the presence of saturated pixels, while PSF shape, nonstellar objects (e.g., background galaxies), and incompleteness may contribute to a slight increase in the ratio at the faintest F150W magnitudes.

5. We compare our NIRCam CMDs to select age and metallicity isochrones from PARSEC models. We find that the models are in generally good agreement with all JWST CMDs, though we find them to be ∼0.05 mag systematically bluer of the lower MS in M92 and Draco II. We posit that this color offset may be due to the complexity of stellar atmospheres in extremely low-mass stars that is currently not well captured in theoretical stellar atmospheres. A notable example includes the known sensitivity of color to the oxygen abundance (e.g., VandenBerg et al. 2022).
6. We compare the photon-noise-based S/Ns for the F090W and F150W magnitudes reported by DOLPHOT for stars in M92 with expectations from v2.0 of the NIRCam ETC. We find they agree within ∼20% over most of the magnitude range, with slightly larger deviations at the very bright and very faint limits. These differences may be due to saturation effects at the bright end and selection effects and/or subtle mismatches between theoretical and observed PSFs at the faint end. We caution that this preliminary comparison does not capture effects such as crowding, which is important in distant dwarf galaxies such as WLM.
7. We are in the process of optimizing DOLPHOT for use with NIRCam and NIRISS. All technical details of the DOLPHOT modules and their application to our ERS data the subject of an upcoming publication on crowded field photometry.

Acknowledgments

The authors thank the anonymous referee for a prompt and big-picture-oriented report. The authors would like to thank David W. Hogg for his input on the program and paper. This work is based on observations made with the NASA/ESA/CSA James Webb Space Telescope. The data were obtained from the Mikulski Archive for Space Telescopes at the Space Telescope Science Institute, which is operated by the Association of Universities for Research in Astronomy, Inc., under NASA contract NAS 5-03127 for JWST. These observations are associated with program DD-ERS-1334. This program also benefits from recent DOLPHOT development work based on observations made with the NASA/ESA Hubble Space Telescope obtained from the Space Telescope Science Institute, which is operated by the Association of Universities for Research in Astronomy, Inc., under NASA contract NAS 526555. These observations are associated with program HST-GO-15902.

Facilities: JWST (NIRCAM), JWST (NIRISS).

ORCID iDs

Daniel R. Weisz https://orcid.org/0000-0002-6442-6030
Kristen B. W. McQuinn https://orcid.org/0000-0001-5538-2614
Alessandro Savino https://orcid.org/0000-0002-1445-4877
Nitya Kallivayalil https://orcid.org/0000-0002-3204-1742
Jay Anderson https://orcid.org/0000-0003-2861-3995
Martha L. Boyer https://orcid.org/0000-0003-4850-9589
Matteo Correnti https://orcid.org/0000-0001-6464-3257
Marla C. Geha https://orcid.org/0000-0002-7007-9725
Andrew E. Dolphin https://orcid.org/0000-0001-8416-4093
Karin M. Sandstrom https://orcid.org/0000-0002-4378-8534
Andrew A. Cole https://orcid.org/0000-0003-0303-3855
Benjamin F. Williams https://orcid.org/0000-0002-7502-0597

Evan D. Skillman https://orcid.org/0000-0003-0605-8732
Roger E. Cohen https://orcid.org/0000-0002-2970-7435
Max J. B. Newman https://orcid.org/0000-0002-8092-2077
Rachael Beaton https://orcid.org/0000-0002-1691-8217
Alessandro Bressan https://orcid.org/0000-0002-7922-8440
Alberto Bolatto https://orcid.org/0000-0002-5480-5686
Michael Boylan-Kolchin https://orcid.org/0000-0002-9604-343X
Alyson M. Brooks https://orcid.org/0000-0002-0372-3736
James S. Bullock https://orcid.org/0000-0003-4298-5082
Charlie Conroy https://orcid.org/0000-0002-1590-8551
M. C. Cooper https://orcid.org/0000-0003-1371-6019
Julianne J. Dalcanton https://orcid.org/0000-0002-1264-2006
Aaron L. Dotter https://orcid.org/0000-0002-4442-5700
Tobias K. Fritz https://orcid.org/0000-0002-3122-300X
Christopher T. Garling https://orcid.org/0000-0001-9061-1697
Mario Gennaro https://orcid.org/0000-0002-5581-2896
Karoline M. Gilbert https://orcid.org/0000-0003-0394-8377
Léo Girardi https://orcid.org/0000-0002-6301-3269
Benjamin D. Johnson https://orcid.org/0000-0002-9280-7594
L. Clifton Johnson https://orcid.org/0000-0001-6421-0953
Jason S. Kalirai https://orcid.org/0000-0001-9690-4159
Evan N. Kirby https://orcid.org/0000-0001-6196-5162
Dustin Lang https://orcid.org/0000-0002-1172-0754
Paola Marigo https://orcid.org/0000-0002-9137-0773
Hannah Richstein https://orcid.org/0000-0002-3188-2718
Edward F. Schlafly https://orcid.org/0000-0002-3569-7421
Judy Schmidt https://orcid.org/0000-0002-2617-5517
Erik J. Tollerud https://orcid.org/0000-0002-9599-310X
Jack T. Warfield https://orcid.org/0000-0003-1634-4644
Andrew Wetzel https://orcid.org/0000-0003-0603-8942

References

Albers, S. M., Weisz, D. R., Cole, A. A., et al. 2019, MNRAS, 490, 5538
Anderson, J., & King, I. R. 2000, PASP, 112, 1360
Bagley, M. B., Finkelstein, S. L., Koekemoer, A. M., et al. 2023, ApJL, 946, L12
Bastian, N., Covey, K. R., & Meyer, M. R. 2010, ARA&A, 48, 339
Battaglia, G., Taibi, S., Thomas, G. F., & Fritz, T. K. 2022, A&A, 657, A54
Baumgardt, H., Faller, J., Meinhold, N., McGovern-Greco, C., & Hilker, M. 2022, MNRAS, 510, 3531
Beaton, R. L., Freedman, W. L., Madore, B. F., et al. 2016, ApJ, 832, 210
Bechtol, K., Drlica-Wagner, A., Balbinot, E., et al. 2015, ApJ, 807, 50
Bianchi, L., Efremova, B., Hodge, P., Massey, P., & Olsen, K. A. G. 2012, AJ, 143, 74
Bono, G., Stetson, P. B., Walker, A. R., et al. 2010, PASP, 122, 651
Boyer, van Loon, J. Th., McDonald, I., et al. 2010, ApJL, 711, L99
Boyer, M. L., McQuinn, K. B. W., Barmby, P., et al. 2015, ApJS, 216, 10
Boyer, M. L., McQuinn, K. B. W., Groenewegen, M. A. T., et al. 2017, ApJ, 851, 152
Boyer, M. L., Williams, B. F., Aringer, B., et al. 2019, ApJ, 879, 109
Boyer, M. L., Woodward, C. E., van Loon, J. T., et al. 2006, AJ, 132, 1415
Boylan-Kolchin, M., & Weisz, D. R. 2021, MNRAS, 505, 2764
Boylan-Kolchin, M., Weisz, D. R., Johnson, B. D., et al. 2015, MNRAS, 453, 1503
Bressan, A., Marigo, P., Girardi, L., et al. 2012, MNRAS, 427, 127
Brown, T. M., Smith, E., Ferguson, H. C., et al. 2006, ApJ, 652, 323
Brown, T. M., Tumlinson, J., Geha, M., et al. 2012, ApJL, 753, L21
Brown, T. M., Tumlinson, J., Geha, M., et al. 2014, ApJ, 796, 91
Bullock, J. S., & Boylan-Kolchin, M. 2017, ARA&A, 55, 343
Buonanno, R., Corsi, C. E., de Biase, G. A., & Ferraro, I. 1979, in Int. Workshop on Image Processing in Astronomy, ed. G. Sedmak, M. Capaccioli, & R. J. Allen (Trieste: Osservatorio Astronomico di Trieste), 354
Campbell, B., Hunter, D. A., Holtzman, J. A., et al. 1992, AJ, 104, 1721
Casey, A. R., & Schlaufman, K. C. 2015, ApJ, 809, 110
Chaboyer, B., Demarque, P., Kernan, P. J., & Krauss, L. M. 1996, Sci, 271, 957
Chabrier, G., Baraffe, I., Allard, F., & Hauschildt, P. 2000, ApJ, 542, 464
Chastenet, J., Sandstrom, K., Chiang, I.-D., et al. 2019, ApJ, 876, 62
Chen, Y., Bressan, A., Girardi, L., et al. 2015, MNRAS, 452, 1068
Choi, J., Dotter, A., Conroy, C., et al. 2016, ApJ, 823, 102
Cole, A. A., Skillman, E. D., Tolstoy, E., et al. 2007, ApJL, 659, L17
Cole, A. A., Weisz, D. R., Dolphin, A. E., et al. 2014, ApJ, 795, 54
Collins, M. L. M., Chapman, S. C., Rich, R. M., et al. 2013, ApJ, 768, 172
Conroy, C. 2013, ARA&A, 51, 393
Conroy, C., Bonaca, A., Cargile, P., et al. 2019, ApJ, 883, 107
Conroy, C., Villaume, A., van Dokkum, P. G., & Lind, K. 2018, ApJ, 854, 139
Correnti, M., Gennaro, M., Kalirai, J. S., Brown, T. M., & Calamida, A. 2016, ApJ, 823, 18
Correnti, M., Gennaro, M., Kalirai, J. S., Cohen, R. E., & Brown, T. M. 2018, ApJ, 864, 147
Dalcanton, J. J., Fouesneau, M., Hogg, D. W., et al. 2015, ApJ, 814, 3
Dalcanton, J. J., Williams, B. F., Lang, D., et al. 2012a, ApJS, 200, 18
Dalcanton, J. J., Williams, B. F., Melbourne, J. L., et al. 2012b, ApJS, 198, 6
Dalcanton, J. J., Williams, B. F., Seth, A. C., et al. 2009, ApJS, 183, 67
Di Valentino, E., Anchordoqui, L. A., Akarsu, Ö, et al. 2021, APh, 131, 102605
Dieball, A., Bedin, L. R., Knigge, C., et al. 2016, ApJ, 817, 48
Dieball, A., Bedin, L. R., Knigge, C., et al. 2019, MNRAS, 486, 2254
Dohm-Palmer, R. C., Skillman, E. D., Gallagher, J., et al. 1998, AJ, 116, 1227
Dolphin, A. E. 2000, PASP, 112, 1383
Dolphin, A. E. 2002, MNRAS, 332, 91
Dolphin, A. E. 2016, ApJ, 825, 153
Dotter, A., Chaboyer, B., Jevremović, D., et al. 2008, ApJS, 178, 89
Dotter, A., Ferguson, J. W., Conroy, C., et al. 2015, MNRAS, 446, 1641
Draine, B. T., & Li, A. 2007, ApJ, 657, 810
Drlica-Wagner, A., Bechtol, K., Rykoff, E. S., et al. 2015, ApJ, 813, 109
Ekström, S., Georgy, C., Eggenberger, P., et al. 2012, A&A, 537, A146
El-Badry, K., Weisz, D. R., & Quataert, E. 2017, MNRAS, 468, 319
El-Badry, K., Wetzel, A., Geha, M., et al. 2016, ApJ, 820, 131
Eldridge, J. J., & Stanway, E. R. 2022, ARA&A, 60, 455
Eldridge, J. J., Stanway, E. R., Xiao, L., et al. 2017, PASA, 34, e058
Escala, I., Gilbert, K. M., Kirby, E. N., et al. 2020, ApJ, 889, 177
Filion, C., Kozhurina-Platais, V., Avila, R. J., Platais, I., & Wyse, R. F. G. 2020, ApJ, 901, 82
Frebel, A., & Norris, J. E. 2015, ARA&A, 53, 631
Freedman, W. L., Hughes, S. M., Madore, B. F., et al. 1994, ApJ, 427, 628
Freedman, W. L., Madore, B. F., Gibson, B. K., et al. 2001, ApJ, 553, 47
Freedman, W. L., Madore, B. F., Hoyt, T., et al. 2020, ApJ, 891, 57
Fritz, T. K., Battaglia, G., Pawlowski, M. S., et al. 2018, A&A, 619, A103
Fu, S. W., Weisz, D. R., Starkenburg, E., et al. 2022, ApJ, 925, 6
Gallart, C., Monelli, M., Mayer, L., et al. 2015, ApJL, 811, L18
Gallart, C., Zoccali, M., & Aparicio, A. 2005, ARA&A, 43, 387
Geha, M., Brown, T. M., Tumlinson, J., et al. 2013, ApJ, 771, 29
Geha, M., Willman, B., Simon, J. D., et al. 2009, ApJ, 692, 1464
Gennaro, M., Geha, M., Tchernyshyov, K., et al. 2018a, ApJ, 863, 38
Gennaro, M., & Robberto, M. 2020, ApJ, 896, 80
Gennaro, M., Tchernyshyov, K., Brown, T. M., et al. 2018b, ApJ, 855, 20
Gilbert, K., Tollerud, E. J., Anderson, J., et al. 2019a, BAAS, 51, 540
Gilbert, K. M., Kalirai, J. S., Guhathakurta, P., et al. 2014, ApJ, 796, 76
Gilbert, K. M., Kirby, E. N., Escala, I., et al. 2019b, ApJ, 883, 128
Gilbert, K. M., Quirk, A. C. N., Guhathakurta, P., et al. 2022, ApJ, 924, 116
Girardi, L., Williams, B. F., Gilbert, K. M., et al. 2010, ApJ, 724, 1030
Gordon, K. D., Bohlin, R., Sloan, G. C., et al. 2022, AJ, 163, 267
Gordon, K. D., Clayton, G. C., Misselt, K. A., Landolt, A. U., & Wolff, M. J. 2003, ApJ, 594, 279
Gordon, K. D., Fouesneau, M., Arab, H., et al. 2016, ApJ, 826, 104
Gordon, K. D., Misselt, K. A., Bouwman, J., et al. 2021, ApJ, 916, 33
Gordon, K. D., Roman-Duval, J., Bot, C., et al. 2014, ApJ, 797, 85
Governato, F., Brook, C., Mayer, L., et al. 2010, Natur, 463, 203
Grebel, E. K., & Gallagher, J. S., III 2004, ApJL, 610, L89
Green, G. M., Schlafly, E., Zucker, C., Speagle, J. S., & Finkbeiner, D. 2019, ApJ, 887, 93
Guhathakurta, P., Yanny, B., Schneider, D. P., & Bahcall, J. N. 1992, AJ, 104, 1790
Gull, M., Weisz, D. R., Senchyna, P., et al. 2022, ApJ, 941, 206
Harris, J., & Zaritsky, D. 2001, ApJS, 136, 25
Harris, W. E. 2010, arXiv:1012.3224
Hayashi, C., & Nakano, T. 1963, PThPh, 30, 460

Hidalgo, S. L., Aparicio, A., Martínez-Delgado, D., & Gallart, C. 2009, ApJ, 705, 704
Hidalgo, S. L., Pietrinferni, A., Cassisi, S., et al. 2018, ApJ, 856, 125
Hjort, A., Zackrisson, E., & Eriksson, K. 2016, 19th Cambridge Workshop on Cool Stars, Stellar Systems, and the Sun (CS19), ed. G. A. Feiden, 40
Holtzman, J. A., Afonso, C., & Dolphin, A. 2006, ApJS, 166, 534
Hunter, D. A., Shaya, E. J., Holtzman, J. A., et al. 1995, ApJ, 448, 179
Ji, A. P., Frebel, A., Chiti, A., & Simon, J. D. 2016, Natur, 531, 610
Jones, O. C., Meixner, M., Justtanont, K., & Glasse, A. 2017, ApJ, 841, 15
Kalirai, J. S., Anderson, J., Dotter, A., et al. 2013, ApJ, 763, 110
Kalirai, J. S., Richer, H. B., Anderson, J., et al. 2012, AJ, 143, 11
Kallivayalil, N., Sales, L. V., Zivick, P., et al. 2018, ApJ, 867, 19
Kallivayalil, N., van der Marel, R. P., Besla, G., Anderson, J., & Alcock, C. 2013, ApJ, 764, 161
Kallivayalil, N., Wetzel, A. R., Simon, J. D., et al. 2015, arXiv:1503.01785
Kirby, E. N., Gilbert, K. M., Escala, I., et al. 2020, AJ, 159, 46
Kirby, E. N., Lanfranchi, G. A., Simon, J. D., Cohen, J. G., & Guhathakurta, P. 2011, ApJ, 727, 78
Koposov, S. E., Belokurov, V., Torrealba, G., & Evans, N. W. 2015, ApJ, 805, 130
Kroupa, P., Weidner, C., Pflamm-Altenburg, J., et al. 2013, in Planets, Stars and Stellar Systems, ed. T. D. Oswalt & G. Gilmore, Vol. 5 (Dordrecht: Springer), 115
Krumholz, M. R. 2014, PhR, 539, 49
Krumholz, M. R., McKee, C. F., & Bland-Hawthorn, J. 2019, ARA&A, 57, 227
Kumar, S. S. 1963, ApJ, 137, 1121
Laevens, B. P. M., Martin, N. F., Bernard, E. J., et al. 2015a, ApJ, 813, 44
Laevens, B. P. M., Martin, N. F., Ibata, R. A., et al. 2015b, ApJ, 802, L18
Laevens, B. P. M., Martin, N. F., Sesar, B., et al. 2014, ApJL, 786, L3
Leaman, R., Cole, A. A., Venn, K. A., et al. 2009, ApJ, 699, 1
Leaman, R., Venn, K. A., Brooks, A. M., et al. 2013, ApJ, 767, 131
Levesque, E. M. 2018, ApJ, 867, 155
Li, T. S., Simon, J. D., Drlica-Wagner, A., et al. 2017, ApJ, 838, 8
Longeard, N., Martin, N., Starkenburg, E., et al. 2018, MNRAS, 480, 2609
Lopez, L. A., Krumholz, M. R., Bolatto, A. D., et al. 2014, ApJ, 795, 121
Lopez, L. A., Krumholz, M. R., Bolatto, A. D., Prochaska, J. X., & Ramirez-Ruiz, E. 2011, ApJ, 731, 91
Madore, B. F., Freedman, W. L., Hatt, D., et al. 2018, ApJ, 858, 11
Maraston, C., Daddi, E., Renzini, A., et al. 2006, ApJ, 652, 85
Marigo, P., Girardi, L., Bressan, A., et al. 2017, ApJ, 835, 77
Marini, E., Dell'Agli, F., Di Criscienzo, M., et al. 2020, MNRAS, 493, 2996
Martin, N. F., Geha, M., Ibata, R. A., et al. 2016, MNRAS, 458, L59
Massey, P. 2003, ARA&A, 41, 15
Mateo, M. L. 1998, ARA&A, 36, 435
McConnachie, A. W. 2012, AJ, 144, 4
McConnachie, A. W., Ibata, R., Martin, N., et al. 2018, ApJ, 868, 55
McKee, C. F., & Ostriker, E. C. 2007, ARA&A, 45, 565
McQuinn, K. B. W., Boyer, M., Skillman, E. D., & Dolphin, A. E. 2019a, ApJ, 880, 63
McQuinn, K. B. W., Boyer, M. L., Mitchell, M. B., et al. 2017a, ApJ, 834, 78
McQuinn, K. B. W., Mao, Y.-Y., Buckley, M. R., et al. 2023, ApJ, 944, 14
McQuinn, K. B. W., Skillman, E. D., Dolphin, A. E., Berg, D., & Kennicutt, R. 2017b, AJ, 154, 51
McQuinn, K. B. W., Skillman, E. D., Dolphin, A. E., & Mitchell, N. P. 2015, ApJ, 808, 109
McQuinn, K. B. W., Skillman, E. D., Heilman, T. N., Mitchell, N. P., & Kelley, T. 2018, MNRAS, 477, 3164
McQuinn, K. B. W., van Zee, L., & Skillman, E. D. 2019b, ApJ, 886, 74
Meixner, M., Galliano, F., Hony, S., et al. 2010, A&A, 518, L71
Melbourne, J., Williams, B. F., Dalcanton, J. J., et al. 2012, ApJ, 748, 47
Melotte, P. J. 1926, MNRAS, 86, 636
Mészáros, S., Masseron, T., García-Hernández, D. A., et al. 2020, MNRAS, 492, 1641
Milone, A. P., Marino, A. F., Bedin, L. R., et al. 2014, MNRAS, 439, 1588
Milone, A. P., Marino, A. F., Bedin, L. R., et al. 2017, MNRAS, 469, 800
Milone, A. P., Marino, A. F., Cassisi, S., et al. 2012, ApJL, 754, L34
Monelli, M., Hidalgo, S. L., Stetson, P. B., et al. 2010, ApJ, 720, 1225
Oey, M. S. 1996, ApJ, 467, 666
Ostriker, E. C., McKee, C. F., & Leroy, A. K. 2010, ApJ, 721, 975
Paresce, F., Shara, M., Meylan, G., et al. 1991, Natur, 352, 297
Patel, E., Kallivayalil, N., Garavito-Camargo, N., et al. 2020, ApJ, 893, 121
Pearson, S., Clark, S. E., Demirjian, A. J., et al. 2022, ApJ, 926, 166
Pellegrini, E. W., Baldwin, J. A., & Ferland, G. J. 2011, ApJ, 738, 34
Peñarrubia, J., Ludlow, A. D., Chanamé, J., & Walker, M. G. 2016, MNRAS, 461, L72
Perrin, M. D., Sivaramakrishnan, A., Lajoie, C.-P., et al. 2014, Proc. SPIE, 9143, 91433X
Piotto, G., Milone, A. P., Bedin, L. R., et al. 2015, AJ, 149, 91
Ricotti, M., & Gnedin, N. Y. 2005, ApJ, 629, 259
Riess, A. G., Macri, L., Casertano, S., et al. 2011, ApJ, 730, 119
Riess, A. G., Macri, L. M., Hoffmann, S. L., et al. 2016, ApJ, 826, 56
Riess, A. G., Yuan, W., Macri, L. M., et al. 2022, ApJL, 934, L7
Rigby, J., Perrin, M., McElwain, M., et al. 2023, PASP, 135, 048001
Rubio, M., Elmegreen, B. G., Hunter, D. A., et al. 2015, Natur, 525, 218
Sacchi, E., Richstein, H., Kallivayalil, N., et al. 2021, ApJL, 920, L19
Salaris, M., Chieffi, A., & Straniero, O. 1993, ApJ, 414, 580
Sana, H., de Mink, S. E., de Koter, A., et al. 2012, Sci, 337, 444
Sarajedini, A., Bedin, L. R., Chaboyer, B., et al. 2007, AJ, 133, 1658
Sarajedini, A., Dotter, A., & Kirkpatrick, A. 2009, ApJ, 698, 1872
Schechter, P. L., Mateo, M., & Saha, A. 1993, PASP, 105, 1342
Schlafly, E. F., Meisner, A. M., Stutz, A. M., et al. 2016, ApJ, 821, 78
Schlaufman, K. C., & Casey, A. R. 2014, ApJ, 797, 13
Schlawin, E., Leisenring, J., Misselt, K., et al. 2020, AJ, 160, 231
Simon, J. D. 2019, ARA&A, 57, 375
Simon, J. D., & Geha, M. 2007, ApJ, 670, 313
Skillman, E. D., Hidalgo, S. L., Weisz, D. R., et al. 2014, ApJ, 786, 44
Skillman, E. D., Monelli, M., Weisz, D. R., et al. 2017, ApJ, 837, 102
Sohn, S. T., Besla, G., van der Marel, R. P., et al. 2013, ApJ, 768, 139
Sohn, S. T., Patel, E., Fardal, M. A., et al. 2020, ApJ, 901, 43
Starkenburg, E., Martin, N., Youakim, K., et al. 2017a, MNRAS, 471, 2587
Starkenburg, E., Oman, K. A., Navarro, J. F., et al. 2017b, MNRAS, 465, 2212
Stetson, P. B. 1987, PASP, 99, 191
Stetson, P. B. 1994, PASP, 106, 250
Stinson, G., Seth, A., Katz, N., et al. 2006, MNRAS, 373, 1074
Stinson, G. S., Dalcanton, J. J., Quinn, T., Kaufmann, T., & Wadsley, J. 2007, ApJ, 667, 170
STScI 2016, JWST User Documentation
Tody, D. 1980, Proc. SPIE, 264, 171
Tolstoy, E. 1996, ApJ, 462, 684
Tolstoy, E., Hill, V., & Tosi, M. 2009, ARA&A, 47, 371
Tosi, M., Greggio, L., & Focardi, P. 1989, Ap&SS, 156, 295
Tully, R. B., Pomarède, D., Graziani, R., et al. 2019, ApJ, 880, 24
Utomo, D., Chiang, I.-D., Leroy, A. K., Sandstrom, K. M., & Chastenet, J. 2019, ApJ, 874, 141
van der Marel, R. P., Fardal, M., Besla, G., et al. 2012, ApJ, 753, 8
VandenBerg, D. A., Bergbusch, P. A., Dotter, A., et al. 2012, ApJ, 755, 15
VandenBerg, D. A., Edvardsson, B., Casagrande, L., & Ferguson, J. W. 2022, MNRAS, 509, 4189
Vargas, L. C., Geha, M., Kirby, E. N., & Simon, J. D. 2013, ApJ, 767, 134
Vargas, L. C., Geha, M. C., & Tollerud, E. J. 2014, ApJ, 790, 73
Venn, K. A., Irwin, M., Shetrone, M. D., et al. 2004, AJ, 128, 1177
Ventura, P., D'Antona, F., Mazzitelli, I., & Gratton, R. 2001, ApJL, 550, L65
Warfield, J. T., Kallivayalil, N., Zivick, P., et al. 2023, MNRAS, 519, 1189
Weisz, D., & Boylan-Kolchin, M. 2019, BAAS, 51, 1
Weisz, D. R., Dolphin, A. E., Skillman, E. D., et al. 2014a, ApJ, 789, 147
Weisz, D. R., Dolphin, A. E., Skillman, E. D., et al. 2014b, ApJ, 789, 148
Wetzel, A. R., Hopkins, P. F., Kim, J.-h., et al. 2016, ApJL, 827, L23
Williams, B. F., Durbin, M. J., Dalcanton, J. J., et al. 2021, ApJS, 253, 53
Williams, B. F., Lang, D., Dalcanton, J. J., et al. 2014, ApJS, 215, 9
Willman, B., & Strader, J. 2012, AJ, 144, 76
Wolf, M. 1909, AN, 183, 187
Yanchulova Merica-Jones, P., Sandstrom, K. M., Johnson, L. C., et al. 2017, ApJ, 847, 102
Yanchulova Merica-Jones, P., Sandstrom, K. M., Johnson, L. C., et al. 2021, ApJ, 907, 50
Ziliotto, T., Milone, A. P., Marino, A. F., et al. 2023, ApJ, 953, 62
Zivick, P., Kallivayalil, N., van der Marel, R. P., et al. 2018, ApJ, 864, 55